Three-dimensional finite difference viscoelastic wave modelling including surface topography

Stig Hestholm

University of Bergen, Department of Solid Earth Physics, Allégaten 41, *N–5007 Bergen, Norway. E-mail: stig.hestholm@ifjf.uib.no*

SUMMARY
I have undertaken 3-D finite difference (FD) modelling of seismic scattering from free-surface topography. Exact free-surface boundary conditions for arbitrary 3-D topographies have been derived for the particle velocities. The boundary conditions are combined with a velocity–stress formulation of the full viscoelastic wave equations. A curved grid represents the physical medium and its upper boundary represents the free-surface topography. The wave equations are numerically discretized by an eighth-order FD method on a staggered grid in space, and a leap-frog technique and the Crank–Nicholson method in time. I simulate scattering from teleseismic *P* waves by using plane incident wave fronts and real topography from a 60×60 km area that includes the NORESS array of seismic receiver stations in southeastern Norway. Synthetic snapshots and seismograms of the wavefield show clear conversion from *P* to *Rg* (short-period fundamental-mode Rayleigh) waves in areas of rough topography, which is consistent with numerous observations. By parallelization on fast supercomputers, it is possible to model higher frequencies and/or larger areas than before.

Key words: finite difference methods, Rayleigh waves, seismic wave propagation, topography, viscoelasticity, wave equation.

INTRODUCTION

Modelling free-surface topography effects is important for seismic profiling on land, whereas in marine settings it is usually sufficient to specify medium parameters without including explicit boundary conditions. However, topography can be important for marine seismics as rough water surfaces can produce scattering that reduces the signal-to-noise ratio. It is, however, the air–solid Earth interface that exhibits the strongest possible impedance contrasts. Modelling topography along such a free surface is important for these reasons. Any irregularities along such a surface would have consequences for the results, the stronger the gradients and/or irregularities the local topography exhibits (Hestholm & Ruud 1998), the greater the effect. Additionally, uncertain or even undetermined parameters such as seismic velocities and densities are used when performing a seismic simulation. On the other hand, topographic data probably have the smallest error margins of any of the model parameters that we use. Also, whenever topographic data are known, they might as well be used in seismic modelling. Performing wave modelling with topography using the method described in this paper involves a few extra terms in the medium equations along with more complicated, but still explicit, boundary conditions for

the particle velocities. Except for the topography data itself, no extra memory is required. In addition, the difference in simulation cost is negligible.

The advantage of modelling with surface topography is that implicit effects such as scattering and conversion will be accounted for automatically in the wavefield synthetics. For example, plane *P* or *S* waves incident on a plane surface of a homogeneous medium cannot convert to *Rg* waves. Also, *P* to *SH* phase conversion depends on surface topography. Amplification and deamplification of propagating waves can be shown to occur at irregularities and in substantial areas around them (Sanchez-Sesma & Campillo 1991). Alluvium-filled irregularly shaped valleys with a plane free surface can generate strong Love and *Rg* waves for some incident waves in three dimensions (Sanchez-Sesma & Luzon 1995). Correspondence with real data is particularly important in earthquake hazard assessment (Pitarka & Irikura 1996).

Rg waves can mask reflections that are the basis of migration. Over the NORESS array in southeastern Norway the *Rg* waves have amplitudes of about 10 per cent of those of the first teleseismic *P*-wave arrivals (see Bannister *et al.* 1990; Gupta *et al.* 1993; Hedlin *et al.* 1991). By quantitatively accounting for these topography effects, a data set better suited for migration can be produced. To illustrate how this might be

used in practice, consider a simulation of an initial earth model with known surface topography. A good correspondence with real data should be obtained to make the initial model viable. Then, using the topography modelling algorithm to propagate the real data backwards in time by a technique such as inverse time migration, good results may be obtained (Sun & McMechan 1992).

The literature on free-surface topography modelling is relatively limited in two dimensions, and even more so in three dimensions. Jih *et al.* (1988) considered different slope types and their combinations explicitly in two dimensions. Another 2-D approach (Robertsson 1996) classified every surface point in a way similar to Jih *et al.* (1988). The scheme can handle both elastic and viscoelastic schemes and implements the field variables at each of seven categories of surface topography points separately. The free-surface conditions are then accounted for by setting all velocities above the surface to zero and using a 'mirror condition' on the normal stress components (Levander 1988). A study that modelled surface topography by the FD method in a 'staircase' manner but using three dimensions was that of Ohminato & Chouet (1997). An interesting 2-D method considered a complete tensorial formulation of the wave equations for modelling curved interfaces and free-surface topography (see Komatitsch *et al.* 1996). This method gives very accurate results and has the advantage of using the same number of spatial partial derivative calculations as for a Cartesian approach. This is 12.5 per cent less in two dimensions and 22.2 per cent less in three dimensions than the chain rule approach used in this study. However, it has the distinct disadvantage of 30 per cent extra memory requirement in two dimensions and 60 per cent extra memory requirement in three dimensions than the general chain rule approach. Additionally, the memory difference will often be even larger because some partial derivatives vanish in the mapping functions due to straight vertical gridlines in most chain rule approaches, as is also the case in the present work. Another procedure is that of Frankel & Leith (1992), who use a 3-D topography modelling algorithm employing a density taper to zero starting at the level of the free surface while keeping the *P* velocity unaltered.

The boundary integral method, or more usually its numerical discretization, the boundary element method, have been used so far only to model relatively simple geometrical features. The reason is that the discretization applied to each structure must be carefully chosen to avoid numerical instabilities. A space–frequency domain representation (see Bouchon *et al.* 1996) calculates the Green functions in the medium for the explicit topography surface under consideration as integrals over horizontal wavenumbers. The diffracted wavefield is the integral over the surface topography of the Green functions multiplied by unknown source density functions. These functions are solved for by the conjugate gradient method. Results are shown for an incident shear wave polarized along the minor and major axes of a cosine-formed ellipse-shaped hill, and Bouchon *et al.* (1996) investigated scattering effects of this hill on the wavefield propagating towards an otherwise plane surface in a homogeneous medium. Sanchez-Sesma & Campillo (1991) also used a boundary integral method to investigate topography effects.

Tessmer & Kosloff (1994) extended their 2-D procedure (see Tessmer *et al.* 1992) for elastic wave modelling with free-surface topography to three dimensions, transforming the velocity–stress formulation of the medium equations from a curved to a rectangular grid. They used a spectral discretization horizontally and a Chebyshev discretization vertically in space. At the free topography surface, the stresses and velocities were transformed into local systems in which the vertical coordinate axis was parallel to the normal of the local surface element. The free-surface conditions were then implemented by a 'characteristic' treatment of both the velocity and the stress components before they were rotated back to the original system. Tessmer & Kosloff (1994) showed results for simple geometrical configurations, but in principle any arbitrary, smooth topography can be incorporated. The present method is based on their method because it transforms the equations of motion from a curved to a rectangular grid. The free-surface boundary conditions, however, are developed in the present work explicitly as an exact, closed set of equations for the 3-D particle velocities.

Day & Minster (1984) were the first to replace the convolutional stress–strain relation for a linear viscoelastic solid (Christensen 1982) with a set of first-order partial differential equations through their Padé approximant method. For constant *Q* over a pre-determined frequency range their approximation yields excellent results. Carcione *et al.* (1988b), however, were the first to represent the convolutional form of the constitutive equations by a first-order system exactly. It was already done for the viscoacoustic case in Carcione *et al.* (1988a) and further developed in Carcione (1993) for 2-D and 3-D displacement–stress formulations of the viscoelastic wave equations. A pseudospectral method was used here for spatial discretization along with a Chebyshev method in time (see Tal-Ezer *et al.* 1990) to minimize numerical dispersion. Robertsson *et al.* (1994) extended the method of Carcione *et al.* (1988b) by exactly representing the convolutional stress–strain relation in the 2-D and 3-D viscoelastic wave equations by a system of first-order partial differential equations for the particle velocities and stresses. They used spatial fourth and temporal second-order FD discretizations. Employing these formulations, Blanch *et al.* (1995) proposed cost-efficient procedures for modelling constant *Q* over a pre-defined frequency range. The immediate advantage of using velocity–stress formulations is that we do not differentiate material parameters across discontinuities (Virieux 1986). Hence, when incorporating our topography boundary conditions in viscoelastic schemes, it is the velocity–stress formulation of Robertsson *et al.* (1994) and the *Q*-modelling procedure of Blanch *et al.* (1995) that I use as starting points. More recently, Xu & McMechan (1998) have presented a more efficient way of modelling full viscoelasticity with an arbitrary number of relaxation mechanisms by reparametrizing the wave equations. By assuming one set of relaxation frequencies for all mechanisms and all parts of the model, they reduced the total number of necessary memory variables from seven to three. This reduces the memory requirement by 40 per cent and the computational time by 25 per cent.

As in Tessmer & Kosloff (1994) and Hestholm & Ruud (1998), a 3-D grid that is curved in the vertical direction is adapted to the surface topography; that is, the top surface of the grid coincides with the surface topography. This method was originally proposed to adapt grids to interior interfaces using pseudospectral spatial derivatives (Fornberg 1988b). I transform the velocity–stress formulation of the viscoelastic, isotropic wave equations (Robertsson *et al.* 1994) from a curved to a rectangular grid, in which the numerical computations are performed. At the topography surface, the velocity boundary

conditions for a free surface are implemented in a local, rotated system at each point of the surface. Each of these systems has its vertical coordinate direction coinciding with the direction of the normal vector of the surface at the point given. The velocity boundary conditions are then rotated back to the Cartesian system before finally being transformed into curved grid equations in a rectangular grid. Once the boundary conditions are given in this grid, the numerical discretization can be performed.

In the following paragraphs, I give the connection between the convolutional stress–strain relation for a linear visco-elastic solid and its first-order partial differential equation representation (Carcione *et al.* 1988a) of velocities and stresses (Robertsson *et al.* 1994). The viscoelastic equivalents to the velocity–stress formulation of the elastic curved grid wave equations (Hestholm & Ruud 1998; Tessmer & Kosloff 1994) will be stated. I show the derivation of free-surface topography boundary conditions as an exact closed system for the particle velocities and give a description of its numerical solution. Next I show a simulation comparison with a geometric example for viscoelastic and elastic cases, as well as a viscoelastic simu-lation of a surface trench. I then present simulated scattering results from teleseismic *P* waves using a plane wave front incident on real topography containing the NORESS array in southeastern Norway. Snapshots and synthetic seismograms of both elastic and viscoelastic wavefields clearly display *Rg* waves in areas of rough topography.

VISCOELASTIC WAVE MODELLING FORMULATION

The basic hypothesis of viscoelastic theory is that the current value of the stress tensor depends upon the history of the strain tensor. This hypothesis can be described as

$$\sigma_{ij} = G_{ijkl} * \dot{\varepsilon}_{kl} = \dot{G}_{ijkl} * \varepsilon_{kl} \tag{1}$$

(Christensen 1982) for a linear isotropic material. $*$ denotes time convolution, and it transforms each strain history, $\dot{\varepsilon}_{ij}(t)$, into the current stress value, $\sigma_{ij}(t)$. The dot denotes time differentiation and G is a fourth-order tensor of time called the relaxation function. For a homogeneous material, G collapses into two independent functions. This is an assumption that is often used also for inhomogeneous materials. Each of these functions is often assumed to have the form of a standard linear solid,

$$G(t) = M_R \left(1 - \sum_{\ell=1}^{L} \left(1 - \frac{\tau_{\varepsilon\ell}}{\tau_{\sigma\ell}} \right) e^{-t/\tau_{\sigma\ell}} \right) \theta(t) \tag{2}$$

(Carcione *et al.* 1988a; Blanch *et al.* 1995). M_R is the relaxation modulus of the medium and $\theta(t)$ is the Heaviside function. The relaxation function $G(t)$ is equivalent to L standard linear solids connected in parallel. Each standard linear solid describes a dashpot and a spring in series in parallel with a spring. $\tau_{\sigma\ell}$ and $\tau_{\varepsilon\ell}$ are the stress and strain relaxation times of the ℓth mechanism.

Following Robertsson *et al.* (1994), the velocity–stress formulation of the viscoelastic wave equations can be derived from the constitutive relation (1) (Appendix A). In three dimensions with one relaxation mechanism (one standard linear solid), this can be written as

$$\rho \frac{\partial u}{\partial t} = \frac{\partial \sigma_{xx}}{\partial x} + \frac{\partial \sigma_{xy}}{\partial y} + \frac{\partial \sigma_{xz}}{\partial z} + f_x, \tag{3}$$

$$\rho \frac{\partial v}{\partial t} = \frac{\partial \sigma_{xy}}{\partial x} + \frac{\partial \sigma_{yy}}{\partial y} + \frac{\partial \sigma_{yz}}{\partial z} + f_y, \tag{4}$$

$$\rho \frac{\partial w}{\partial t} = \frac{\partial \sigma_{xz}}{\partial x} + \frac{\partial \sigma_{yz}}{\partial y} + \frac{\partial \sigma_{zz}}{\partial z} + f_z, \tag{5}$$

$$\frac{\partial \sigma_{xx}}{\partial t} = \pi \frac{\tau_\varepsilon^P}{\tau_\sigma} \left(\frac{\partial u}{\partial x} + \frac{\partial v}{\partial y} + \frac{\partial w}{\partial z} \right) - 2\mu \frac{\tau_\varepsilon^S}{\tau_\sigma} \left(\frac{\partial v}{\partial y} + \frac{\partial w}{\partial z} \right) + r_{xx}, \tag{6}$$

$$\frac{\partial \sigma_{yy}}{\partial t} = \pi \frac{\tau_\varepsilon^P}{\tau_\sigma} \left(\frac{\partial u}{\partial x} + \frac{\partial v}{\partial y} + \frac{\partial w}{\partial z} \right) - 2\mu \frac{\tau_\varepsilon^S}{\tau_\sigma} \left(\frac{\partial u}{\partial x} + \frac{\partial w}{\partial z} \right) + r_{yy}, \tag{7}$$

$$\frac{\partial \sigma_{zz}}{\partial t} = \pi \frac{\tau_\varepsilon^P}{\tau_\sigma} \left(\frac{\partial u}{\partial x} + \frac{\partial v}{\partial y} + \frac{\partial w}{\partial z} \right) - 2\mu \frac{\tau_\varepsilon^S}{\tau_\sigma} \left(\frac{\partial u}{\partial x} + \frac{\partial v}{\partial y} \right) + r_{zz}, \tag{8}$$

$$\frac{\partial \sigma_{xy}}{\partial t} = \mu \frac{\tau_\varepsilon^S}{\tau_\sigma} \left(\frac{\partial u}{\partial y} + \frac{\partial v}{\partial x} \right) + r_{xy}, \tag{9}$$

$$\frac{\partial \sigma_{xz}}{\partial t} = \mu \frac{\tau_\varepsilon^S}{\tau_\sigma} \left(\frac{\partial u}{\partial z} + \frac{\partial w}{\partial x} \right) + r_{xz}, \tag{10}$$

$$\frac{\partial \sigma_{yz}}{\partial t} = \mu \frac{\tau_\varepsilon^S}{\tau_\sigma} \left(\frac{\partial v}{\partial z} + \frac{\partial w}{\partial y} \right) + r_{yz}, \tag{11}$$

$$\frac{\partial r_{xx}}{\partial t} = -\frac{1}{\tau_\sigma} \left\{ r_{xx} + \pi \left(\frac{\tau_\varepsilon^P}{\tau_\sigma} - 1 \right) \left(\frac{\partial u}{\partial x} + \frac{\partial v}{\partial y} + \frac{\partial w}{\partial z} \right) \right.$$
$$\left. - 2\mu \left(\frac{\tau_\varepsilon^S}{\tau_\sigma} - 1 \right) \left(\frac{\partial v}{\partial y} + \frac{\partial w}{\partial z} \right) \right\}, \tag{12}$$

$$\frac{\partial r_{yy}}{\partial t} = -\frac{1}{\tau_\sigma} \left\{ r_{yy} + \pi \left(\frac{\tau_\varepsilon^P}{\tau_\sigma} - 1 \right) \left(\frac{\partial u}{\partial x} + \frac{\partial v}{\partial y} + \frac{\partial w}{\partial z} \right) \right.$$
$$\left. - 2\mu \left(\frac{\tau_\varepsilon^S}{\tau_\sigma} - 1 \right) \left(\frac{\partial u}{\partial x} + \frac{\partial w}{\partial z} \right) \right\}, \tag{13}$$

$$\frac{\partial r_{zz}}{\partial t} = -\frac{1}{\tau_\sigma} \left\{ r_{zz} + \pi \left(\frac{\tau_\varepsilon^P}{\tau_\sigma} - 1 \right) \left(\frac{\partial u}{\partial x} + \frac{\partial v}{\partial y} + \frac{\partial w}{\partial z} \right) \right.$$
$$\left. - 2\mu \left(\frac{\tau_\varepsilon^S}{\tau_\sigma} - 1 \right) \left(\frac{\partial u}{\partial x} + \frac{\partial v}{\partial y} \right) \right\}, \tag{14}$$

$$\frac{\partial r_{xy}}{\partial t} = -\frac{1}{\tau_\sigma} \left\{ r_{xy} + \mu \left(\frac{\tau_\varepsilon^S}{\tau_\sigma} - 1 \right) \left(\frac{\partial u}{\partial y} + \frac{\partial v}{\partial x} \right) \right\}, \tag{15}$$

$$\frac{\partial r_{xz}}{\partial t} = -\frac{1}{\tau_\sigma} \left\{ r_{xz} + \mu \left(\frac{\tau_\varepsilon^S}{\tau_\sigma} - 1 \right) \left(\frac{\partial u}{\partial z} + \frac{\partial w}{\partial x} \right) \right\}, \tag{16}$$

$$\frac{\partial r_{yz}}{\partial t} = -\frac{1}{\tau_\sigma} \left\{ r_{yz} + \mu \left(\frac{\tau_\varepsilon^S}{\tau_\sigma} - 1 \right) \left(\frac{\partial v}{\partial z} + \frac{\partial w}{\partial y} \right) \right\}, \tag{17}$$

where ρ is the density, π is the relaxation modulus for *P* waves, $\pi = \lambda + 2\mu$ (λ and μ are the Lamé parameters), and μ is the relaxation modulus for *S* waves as in the elastic case. τ_ε^P and τ_ε^S are the strain relaxation times for *P* and *S* waves respectively, and τ_σ is the stress relaxation time. The same τ_σ can be used both for *P* and *S* waves (Blanch *et al.* 1995). f_x, f_y and f_z are the components of the body forces, *u*, *v* and *w* are the particle velocity components and σ_{xx}, σ_{yy}, σ_{zz}, σ_{xy}, σ_{xz} and σ_{yz} are the stress components. r_{xx}, r_{yy}, r_{zz}, r_{xy}, r_{xz} and r_{yz} are the components of the memory variables. These are the equations

governing wave propagation in a linear isotropic viscoelastic medium, and they are the equations of motion, the stress–strain relation and the memory variable equations.

I introduce a linear mapping from a rectangular (ξ, κ, η)-system (Fig. 1) to a curved grid in the (x, y, z)-system (Fig. 2), where both systems are positive upwards for the vertical coordinate. The 3-D mapping can be written as

$$x(\xi, \kappa, \eta) = \xi, \tag{18}$$

$$y(\xi, \kappa, \eta) = \kappa, \tag{19}$$

$$z(\xi, \kappa, \eta) = \frac{\eta}{\eta_{\max}} z_0(\xi, \kappa), \tag{20}$$

where $z_0(\xi, \kappa)$ is the topography function, and the rectangular (ξ, κ, η)-system is bounded by $\xi = 0$, $\xi = \xi_{\max}$, $\kappa = 0$, $\kappa = \kappa_{\max}$, $\eta = 0$ and $\eta = \eta_{\max}$. For the curved grid in the (x, y, z)-system, the extent of stretching is proportional to the distance from the bottom plane of the grid $(z = 0)$. From eqs (18)–(20) we obtain, for a differentiable function $f(x, y, z)$,

$$\frac{\partial f}{\partial x} = \frac{\partial f}{\partial \xi} + \frac{\partial f}{\partial \eta} \frac{\partial \eta}{\partial x}, \tag{21}$$

$$\frac{\partial f}{\partial y} = \frac{\partial f}{\partial \kappa} + \frac{\partial f}{\partial \eta} \frac{\partial \eta}{\partial y}, \tag{22}$$

$$\frac{\partial f}{\partial z} = \frac{\partial f}{\partial \eta} \frac{\partial \eta}{\partial z}. \tag{23}$$

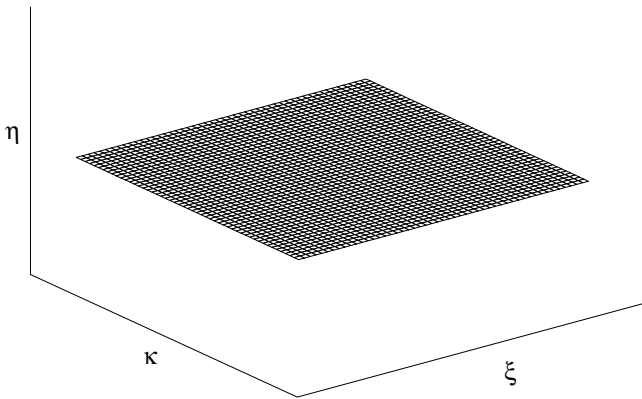Expressions for the partial derivatives, which are needed in the medium equations, are found from eqs (18)–(20) (see
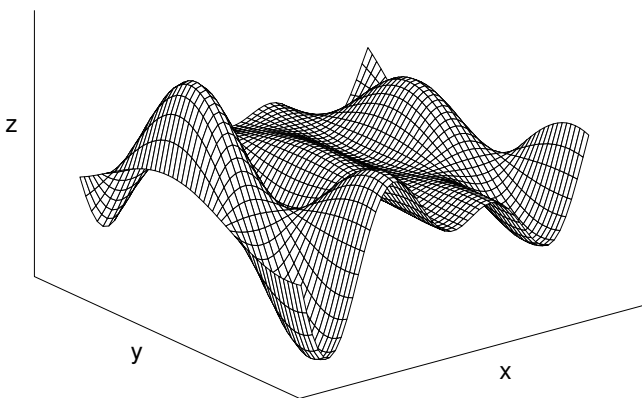

Figure 1. Rectangular grid surface.

Figure 2. Curved grid surface.

Appendix B):

$$\frac{\partial \xi}{\partial x} = 1, \quad \frac{\partial \xi}{\partial y} = 0, \quad \frac{\partial \xi}{\partial z} = 0, \tag{24}$$

$$\frac{\partial \kappa}{\partial x} = 0, \quad \frac{\partial \kappa}{\partial y} = 1, \quad \frac{\partial \kappa}{\partial z} = 0, \tag{25}$$

$$A(\xi, \kappa, \eta) = \frac{\partial \eta}{\partial x} = -\frac{\eta}{z_0(\xi, \kappa)} \frac{\partial z_0(\xi, \kappa)}{\partial \xi}, \tag{26}$$

$$B(\xi, \kappa, \eta) = \frac{\partial \eta}{\partial y} = -\frac{\eta}{z_0(\xi, \kappa)} \frac{\partial z_0(\xi, \kappa)}{\partial \kappa}, \tag{27}$$

$$C(\xi, \kappa) = \frac{\partial \eta}{\partial z} = \frac{\eta_{\max}}{z_0(\xi, \kappa)}. \tag{28}$$

The velocity–stress formulation of the equations of motion, Hooke's law and the memory variable equations is given in the curved grid in the (x, y, z)-system by eqs (3)–(17). Expanding these by the chain rule (Appendix C) as for the elastic cases in Hestholm & Ruud (1994, 1998) and substituting for $\partial \eta / \partial x$, $\partial \eta / \partial y$ and $\partial \eta / \partial z$, I obtain the medium equations with one relaxation mechanism in the rectangular (ξ, κ, η)-system:

$$\rho \frac{\partial u}{\partial t} = \frac{\partial \sigma_{xx}}{\partial \xi} + A(\xi, \kappa, \eta) \frac{\partial \sigma_{xx}}{\partial \eta} + \frac{\partial \sigma_{xy}}{\partial \kappa} + B(\xi, \kappa, \eta) \frac{\partial \sigma_{xy}}{\partial \eta}$$
$$+ C(\xi, \kappa) \frac{\partial \sigma_{xz}}{\partial \eta} + f_x, \tag{29}$$

$$\rho \frac{\partial v}{\partial t} = \frac{\partial \sigma_{xy}}{\partial \xi} + A(\xi, \kappa, \eta) \frac{\partial \sigma_{xy}}{\partial \eta} + \frac{\partial \sigma_{yy}}{\partial \kappa} + B(\xi, \kappa, \eta) \frac{\partial \sigma_{yy}}{\partial \eta}$$
$$+ C(\xi, \kappa) \frac{\partial \sigma_{yz}}{\partial \eta} + f_y, \tag{30}$$

$$\rho \frac{\partial w}{\partial t} = \frac{\partial \sigma_{xz}}{\partial \xi} + A(\xi, \kappa, \eta) \frac{\partial \sigma_{xz}}{\partial \eta} + \frac{\partial \sigma_{yz}}{\partial \kappa} + B(\xi, \kappa, \eta) \frac{\partial \sigma_{yz}}{\partial \eta}$$
$$+ C(\xi, \kappa) \frac{\partial \sigma_{zz}}{\partial \eta} + f_z, \tag{31}$$

$$\frac{\partial \sigma_{xx}}{\partial t} = \pi \frac{\tau_\varepsilon^P}{\tau_\sigma} \left(\frac{\partial u}{\partial \xi} + A(\xi, \kappa, \eta) \frac{\partial u}{\partial \eta} + \frac{\partial v}{\partial \kappa} \right.$$
$$\left. + B(\xi, \kappa, \eta) \frac{\partial v}{\partial \eta} + C(\xi, \kappa) \frac{\partial w}{\partial \eta} \right)$$
$$- 2\mu \frac{\tau_\varepsilon^S}{\tau_\sigma} \left(\frac{\partial v}{\partial \kappa} + B(\xi, \kappa, \eta) \frac{\partial v}{\partial \eta} + C(\xi, \kappa) \frac{\partial w}{\partial \eta} \right) + r_{xx}, \tag{32}$$

$$\frac{\partial \sigma_{yy}}{\partial t} = \pi \frac{\tau_\varepsilon^P}{\tau_\sigma} \left(\frac{\partial u}{\partial \xi} + A(\xi, \kappa, \eta) \frac{\partial u}{\partial \eta} + \frac{\partial v}{\partial \kappa} \right.$$
$$\left. + B(\xi, \kappa, \eta) \frac{\partial v}{\partial \eta} + C(\xi, \kappa) \frac{\partial w}{\partial \eta} \right)$$
$$- 2\mu \frac{\tau_\varepsilon^S}{\tau_\sigma} \left(\frac{\partial u}{\partial \xi} + A(\xi, \kappa, \eta) \frac{\partial u}{\partial \eta} + C(\xi, \kappa) \frac{\partial w}{\partial \eta} \right) + r_{yy}, \tag{33}$$

$$\frac{\partial \sigma_{zz}}{\partial t} = \pi \frac{\tau_\varepsilon^P}{\tau_\sigma} \left(\frac{\partial u}{\partial \xi} + A(\xi, \kappa, \eta) \frac{\partial u}{\partial \eta} + \frac{\partial v}{\partial \kappa} \right.$$
$$\left. + B(\xi, \kappa, \eta) \frac{\partial v}{\partial \eta} + C(\xi, \kappa) \frac{\partial w}{\partial \eta} \right)$$
$$- 2\mu \frac{\tau_\varepsilon^S}{\tau_\sigma} \left(\frac{\partial u}{\partial \xi} + A(\xi, \kappa, \eta) \frac{\partial u}{\partial \eta} + \frac{\partial v}{\partial \kappa} + B(\xi, \kappa, \eta) \frac{\partial v}{\partial \eta} \right) + r_{zz},$$
$$\tag{34}$$

$$\frac{\partial \sigma_{xy}}{\partial t} = \mu \frac{\tau_\varepsilon^S}{\tau_\sigma}\left(\frac{\partial u}{\partial \kappa} + B(\xi, \kappa, \eta)\frac{\partial u}{\partial \eta} + \frac{\partial v}{\partial \xi} + A(\xi, \kappa, \eta)\frac{\partial v}{\partial \eta}\right) + r_{xy},$$

(35)

$$\frac{\partial \sigma_{xz}}{\partial t} = \mu \frac{\tau_\varepsilon^S}{\tau_\sigma}\left(C(\xi, \kappa)\frac{\partial u}{\partial \eta} + \frac{\partial w}{\partial \xi} + A(\xi, \kappa, \eta)\frac{\partial w}{\partial \eta}\right) + r_{xz},$$

(36)

$$\frac{\partial \sigma_{yz}}{\partial t} = \mu \frac{\tau_\varepsilon^S}{\tau_\sigma}\left(C(\xi, \kappa)\frac{\partial v}{\partial \eta} + \frac{\partial w}{\partial \kappa} + B(\xi, \kappa, \eta)\frac{\partial w}{\partial \eta}\right) + r_{yz},$$

(37)

$$\frac{\partial r_{xx}}{\partial t} = -\frac{1}{\tau_\sigma}\left\{r_{xx} + \pi\left(\frac{\tau_\varepsilon^P}{\tau_\sigma} - 1\right)\left[\frac{\partial u}{\partial \xi} + A(\xi, \kappa, \eta)\frac{\partial u}{\partial \eta}\right.\right.$$
$$\left. + \frac{\partial v}{\partial \kappa} + B(\xi, \kappa, \eta)\frac{\partial v}{\partial \eta} + C(\xi, \kappa)\frac{\partial w}{\partial \eta}\right] - 2\mu\left(\frac{\tau_\varepsilon^S}{\tau_\sigma} - 1\right)$$
$$\left. \times \left(\frac{\partial v}{\partial \kappa} + B(\xi, \kappa, \eta)\frac{\partial v}{\partial \eta} + C(\xi, \kappa)\frac{\partial w}{\partial \eta}\right)\right\},$$

(38)

$$\frac{\partial r_{yy}}{\partial t} = -\frac{1}{\tau_\sigma}\left\{r_{yy} + \pi\left(\frac{\tau_\varepsilon^P}{\tau_\sigma} - 1\right)\left[\frac{\partial u}{\partial \xi} + A(\xi, \kappa, \eta)\frac{\partial u}{\partial \eta}\right.\right.$$
$$\left. + \frac{\partial v}{\partial \kappa} + B(\xi, \kappa, \eta)\frac{\partial v}{\partial \eta} + C(\xi, \kappa)\frac{\partial w}{\partial \eta}\right] - 2\mu\left(\frac{\tau_\varepsilon^S}{\tau_\sigma} - 1\right)$$
$$\left. \times \left(\frac{\partial u}{\partial \xi} + A(\xi, \kappa, \eta)\frac{\partial u}{\partial \eta} + C(\xi, \kappa)\frac{\partial w}{\partial \eta}\right)\right\},$$

(39)

$$\frac{\partial r_{zz}}{\partial t} = -\frac{1}{\tau_\sigma}\left\{r_{zz} + \pi\left(\frac{\tau_\varepsilon^P}{\tau_\sigma} - 1\right)\left[\frac{\partial u}{\partial \xi} + A(\xi, \kappa, \eta)\frac{\partial u}{\partial \eta} + \frac{\partial v}{\partial \kappa}\right.\right.$$
$$\left. + B(\xi, \kappa, \eta)\frac{\partial v}{\partial \eta} + C(\xi, \kappa)\frac{\partial w}{\partial \eta}\right] - 2\mu\left(\frac{\tau_\varepsilon^S}{\tau_\sigma} - 1\right)$$
$$\left. \times \left(\frac{\partial u}{\partial \xi} + A(\xi, \kappa, \eta)\frac{\partial u}{\partial \eta} + \frac{\partial v}{\partial \kappa} + B(\xi, \kappa, \eta)\frac{\partial v}{\partial \eta}\right)\right\},$$

(40)

$$\frac{\partial r_{xy}}{\partial t} = -\frac{1}{\tau_\sigma}\left\{r_{xy} + \mu\left(\frac{\tau_\varepsilon^S}{\tau_\sigma} - 1\right)\right.$$
$$\left. \times \left(\frac{\partial u}{\partial \kappa} + B(\xi, \kappa, \eta)\frac{\partial u}{\partial \eta} + \frac{\partial v}{\partial \xi} + A(\xi, \kappa, \eta)\frac{\partial v}{\partial \eta}\right)\right\},$$

(41)

$$\frac{\partial r_{xz}}{\partial t} = -\frac{1}{\tau_\sigma}\left\{r_{xz} + \mu\left(\frac{\tau_\varepsilon^S}{\tau_\sigma} - 1\right)\right.$$
$$\left. \times \left(C(\xi, \kappa)\frac{\partial u}{\partial \eta} + \frac{\partial w}{\partial \xi} + A(\xi, \kappa, \eta)\frac{\partial w}{\partial \eta}\right)\right\},$$

(42)

$$\frac{\partial r_{yz}}{\partial t} = -\frac{1}{\tau_\sigma}\left\{r_{yz} + \mu\left(\frac{\tau_\varepsilon^S}{\tau_\sigma} - 1\right)\right.$$
$$\left. \times \left(C(\xi, \kappa)\frac{\partial v}{\partial \eta} + \frac{\partial w}{\partial \kappa} + B(\xi, \kappa, \eta)\frac{\partial w}{\partial \eta}\right)\right\}.$$

(43)

Eqs (29)–(43) are the momentum conservation equations, Hooke's law and the memory variable equations given in the rectangular (ξ, κ, η)-grid.

FREE SURFACE BOUNDARY CONDITIONS

The 3-D free boundary conditions for the particle velocities at a locally horizontal surface (or in a system where the z-axis is parallel to the local normal vector of the surface) resulting from the vanishing stress condition can be written as

$$\frac{\partial u}{\partial z} = -\frac{\partial w}{\partial x},$$

(44)

$$\frac{\partial v}{\partial z} = -\frac{\partial w}{\partial y},$$

(45)

$$\frac{\partial w}{\partial z} = -\frac{\lambda}{\lambda + 2\mu}\left(\frac{\partial u}{\partial x} + \frac{\partial v}{\partial y}\right),$$

(46)

with x and y the horizontal coordinates and z the vertical coordinate. We want to apply these conditions to a topography surface. At each surface point, I introduce a local coordinate system (x', y', z'), in which the z'-axis coincides with the local normal vector direction of the surface. In this local system I impose the conditions (44)–(46). Once this is done, they have to be rotated back to the Cartesian (x, y, z)-system. This rotation is expressed by $\mathbf{v} = \mathbf{A}^{-1}\mathbf{v}'$, i.e.

$$\mathbf{v}' = \mathbf{A}\mathbf{v},$$

(47)

where $\mathbf{v}$ and $\mathbf{v}'$ are the particle velocity vectors in the (x, y, z)- and the (x', y', z')-systems respectively. $\mathbf{A}$ is the rotation matrix, which can be given by

$$\mathbf{A} = \begin{pmatrix} \cos\theta & 0 & \sin\theta \\ -\sin\theta\sin\phi & \cos\phi & \cos\theta\sin\phi \\ -\sin\theta\cos\phi & -\sin\phi & \cos\theta\cos\phi \end{pmatrix},$$

(48)

where θ is the rotation angle between the x-axis and the local x'-axis in the (x, z)-plane and ϕ is the rotation angle between the y-axis and the local y'-axis in the local (y', z')-plane. We also have the relations $\tan\theta = \partial z_0(\xi, \kappa)/\partial\xi$ and $\tan\phi = \partial z_0(\xi, \kappa)/\partial\kappa \cos\theta$, now expressed in the computational (ξ, κ, η)-grid (see Appendix D).

The calculations of the rotation from the local (x', y', z')-system back to the Cartesian (x, y, z)-system can be performed as in Appendix D. Once this is done, a transformation from the Cartesian (x, y, z)-system to the computational (ξ, κ, η)-grid should be performed (Appendix D) to express the boundary conditions as curved grid equations in the rectangular, computational (ξ, κ, η)-grid. This is achieved by using the chain rule in the same way as was done for the medium equations. I arrive at the 3-D boundary conditions for free-surface

topography given in the computational (ξ, κ, η)-grid by

$$\frac{1}{e^2}(1+p^2)C(\xi,\kappa)\frac{\partial u}{\partial \eta} + \frac{d}{e^2}(1+p^2)C(\xi,\kappa)\frac{\partial w}{\partial \eta}$$

$$= 2d\frac{\partial u}{\partial \xi} + \frac{p}{e}\frac{\partial v}{\partial \xi} + (d^2-1)\frac{\partial w}{\partial \xi} + \frac{p}{e}\frac{\partial u}{\partial \kappa} + \frac{dp}{e}\frac{\partial w}{\partial \kappa}, \qquad (49)$$

$$-\frac{fp}{e^2}(1+p^2)C(\xi,\kappa)\frac{\partial u}{\partial \eta} + \frac{1}{e^2}(1+p^2)C(\xi,\kappa)\frac{\partial v}{\partial \eta}$$

$$+\frac{p}{e}(1+p^2)C(\xi,\kappa)\frac{\partial w}{\partial \eta}$$

$$= -2dfp\frac{\partial u}{\partial \xi} + d(1-p^2)\frac{\partial v}{\partial \xi} + 2fp\frac{\partial w}{\partial \xi} + d(1-p^2)\frac{\partial u}{\partial \kappa}$$

$$+2\frac{p}{e}\frac{\partial v}{\partial \kappa} + (p^2-1)\frac{\partial w}{\partial \kappa}, \qquad (50)$$

$$\frac{d}{e^2}(1+p^2)C(\xi,\kappa)\frac{\partial u}{\partial \eta} + \frac{p}{e^3}(1+p^2)C(\xi,\kappa)\frac{\partial v}{\partial \eta}$$

$$-\frac{1}{e^2}(1+p^2)C(\xi,\kappa)\frac{\partial w}{\partial \eta}$$

$$= \left\{ \zeta\left(1+\frac{p^2}{e^2}\right) + d^2 \right\}\frac{\partial u}{\partial \xi} - \frac{dp}{e}(\zeta-1)\frac{\partial v}{\partial \xi} + d(\zeta-1)\frac{\partial w}{\partial \xi}$$

$$-\frac{dp}{e}(\zeta-1)\frac{\partial u}{\partial \kappa} + \frac{1}{e^2}(\zeta+p^2)\frac{\partial v}{\partial \kappa} + \frac{p}{e}(\zeta-1)\frac{\partial w}{\partial \kappa}, \qquad (51)$$

using definition (28) and

$$\zeta = \frac{\lambda}{\lambda+2\mu}, \qquad (52)$$

$$d = \frac{\partial z_0(\xi,\kappa)}{\partial \xi} = \tan\theta, \qquad (53)$$

$$e = \cos[\arctan(d)] = \cos\theta, \qquad (54)$$

$$f = \sin[\arctan(d)] = \sin\theta, \qquad (55)$$

$$p = \frac{\partial z_0(\xi,\kappa)}{\partial \kappa} e = \tan\phi. \qquad (56)$$

Eqs (49)–(56) are exact 3-D boundary conditions for an arbitrary, smooth free-surface topography. They result from rotating the velocity free-surface conditions from local systems at each point of the surface topography into a Cartesian system before transforming them into curved grid equations in the computational grid (Appendix D). The boundary conditions (49)–(56) are obviously not restricted to the FD method or any other numerical discretization technique.

NUMERICAL DISCRETIZATION

To discretize the viscoelastic wave equations (29)–(43), high-order, cost-optimized FD operators were used (see Kindelan *et al.* 1990). Their method of optimal FD coefficients from minimization of the total simulation cost under the constraint of a pre-defined maximum numerical dispersion is based on the work of Holberg (1987). The schemes employ a staggered discretization stencil of the velocity–stress formulation of the viscoelastic wave equations as was employed for the elasto-dynamic wave equations in Levander (1988) and Virieux (1986). An advantage of using a staggered definition of variables is that we can avoid explicit definition of stresses at the surface

topography as it suffices to define the velocities there. In order to obtain the velocities and stresses explicitly defined at each time step, I stagger the vertical particle velocity component w one half-grid length downwards. Generally, u is staggered one half-grid length in the positive ξ-direction, v is staggered one half-grid length in the positive κ-direction and w is staggered one half-grid length in the negative η-direction (downwards). The stresses and the memory variables are defined either at the gridpoints (σ_{xx}, σ_{yy}, σ_{zz}, r_{xx}, r_{yy} and r_{zz}), or at the midpoint of the grid rectangles (σ_{xy}, σ_{xz}, σ_{yz}, r_{xy}, r_{xz} and r_{yz}), that is, one half-grid length positively in each of the directions of their indices. The 3-D boundary conditions, eqs (49)–(51), are discretized by second-order staggered FD operators. Below the free surface, the central, staggered FD method's order (Fornberg 1988a) is gradually increased with depth, via fourth and sixth up to eighth order; the latter is the method used inside the domain and it is dispersion-bounded and cost-optimized (Kindelan *et al.* 1990).

To extrapolate velocities and stresses in time, the (second-order) leapfrog technique is used. The equations for the memory variables r_{ij} might become stiff for τ_σ small compared to the time step Δt; therefore, the Crank–Nicholson stiff solver was used to propagate the memory variables in time (Robertsson *et al.* 1994). Since the memory variable equations are first-order ordinary differential equations, the usually implicit Crank–Nicholson scheme becomes explicit, and only marginally more expensive than conventional explicit schemes. The Crank–Nicholson scheme is unconditionally stable.

Blanch *et al.* (1995) described a method for approximating a constant Q over a pre-determined frequency interval for an arbitrary number of L standard linear solids. However, both in the present work and in Robertsson *et al.* (1994), only one standard linear solid (relaxation mechanism) is used, and then a simpler method can be employed. Looking at the curves for Q versus frequency for one relaxation mechanism (Blanch *et al.* 1995), we see that these curves are symmetric about a minimum Q. The method I use is to set the desired Q equal to this minimum value for the central frequency of the source and calculate τ_σ, τ_ϵ^P and τ_ϵ^S accordingly, possibly with a different Q for P and S waves. This procedure was used in Robertsson *et al.* (1994) and ensures a symmetric behaviour of the attenuation and dispersion about the source's central frequency. The expressions for the relaxation times resulting from this principle are

$$\tau_\sigma = \frac{1}{\omega}\left(\sqrt{1+\frac{1}{Q_P^2}} - \frac{1}{Q_P} \right), \qquad (57)$$

$$\tau_\epsilon^P = \frac{1}{\omega^2 \tau_\sigma}, \qquad (58)$$

$$\tau_\epsilon^S = \frac{1+\omega\tau_\sigma Q_S}{\omega Q_S - \omega^2 \tau_\sigma}, \qquad (59)$$

with $\omega = 2\pi f$, where f is the central frequency, and Q_P and Q_S are Q-values for the P and S waves respectively.

For the viscoelastic modelling examples I found the following procedure to work best to absorb waves along the grid boundaries. First I calculated τ_σ, τ_ϵ^P and τ_ϵ^S from the above formulae with $Q_P = 2.5$ and $Q_S = 2.0$. I then set τ_σ to a very high value, i.e. $\tau_\sigma \sim 100$, thereby attaining a much higher order of magnitude of the stress relaxation time than the strain relaxation times. For the elastic examples shown I

used exponential damping according to Cerjan *et al.* (1985). The stresses and velocities were multiplied by exponentially decreasing terms towards the artificial boundaries. The thickness of the absorbing layers was 30 gridpoints for both the viscoelastic and the elastic examples with real topography, which corresponds to 2.5 times the dominant wavelength of the source. In the viscoelastic case, 20 of these gridpoints were used for a linear tapering of the relaxation times towards their values along the boundaries.

To find the particle velocity components at the surface topography from the closed system (49)–(51), I solve it directly and simultaneously as a linear system with respect to the velocities at the surface as they are defined in the second-order vertical derivative discretizations. In this procedure, the horizontal partial derivatives are calculated one grid length and one-and-a-half grid lengths below the free surface and considered known from the medium equations. The resulting linear system of equations for the unknown particle velocities at the free surface has the determinant

$$D = \frac{1}{e^6}(1+p^2)^4(1+d^2)C^3(\xi, \kappa),\tag{60}$$

using definitions (28) and (52)–(56). This determinant is always positive and its minimum value is $C^3(\xi, \kappa)$, which occurs for a plane surface. Therefore, this numerical solution of boundary conditions (49)–(51) is unconditionally stable.

SIMPLE TOPOGRAPHIES

Figs 3–5 show snapshots of the initial shotpoint of a Ricker *P* source with a central frequency of 5 Hz in the focus of a 3-D parabola (Fig. 3) and reflected waves from its surface ($t = 1.4$ s) for an elastic (Fig. 4) and a corresponding viscoelastic case (Fig. 5). The snapshots are taken along the vertical diagonal (from small ξ and κ to large ξ and κ) and the vertical particle velocity component w is displayed. According to the analytic solution the reflected wave in the elastic case should be perfectly plane and in the viscoelastic case it should have a plane appearance. This is seen to be the case in Figs 4 and 5. The *P*- and *S*-wave velocities of the homogeneous medium are 5.0 and 2.89 km s^{-1} respectively and the density is 2000 kg m^{-3}. The viscoelastic *Q*-value is 20 for both *P* and *S* waves and the rectangular grid in each case has size of $127 \times 127 \times 127$ with a uniform grid distance of 0.1 km. The maximum medium height (at the top of the parabola) is 12.6 km and the focal point is 3 km below it (the focal point defines the curvature of the parabola). The central frequency of 5 Hz is high enough in these cases for a visible difference between the elastic and viscoelastic cases to appear. The intrinsic attenuation causes the viscoelastic reflection to have a smoother appearance and the physical dispersion leads to a broader wave front. This dispersion combined with the high medium velocity leads the viscoelastic wave front to propagate noticeably further than the corresponding elastic wave front in the same time. The snapshots of Figs 4 and 5 are scaled individually according to their maximum value to enhance the features of each case.

Next I show results from a south–north-oriented 1-D trench at the middle position of the west–east direction of the domain (Fig. 6). With slight modifications of parameters (most significant with respect to scale) this example can be compared with the simulation of the same geometry in Tessmer & Kosloff (1994). A point *P* source is located at the surface 40 km from the south and 40 km from the west grid edges. The domain is 60 km $\times$ 60 km $\times$ 20 km with a uniform grid distance of 0.2 km, i.e. $300 \times 300 \times 100$ gridpoints. The south–north-oriented trench has both a depth and a width of 1.2 km, which is half the dominant wavelength of the Ricker source of central frequency 2.5 Hz. The medium is homogeneous with a
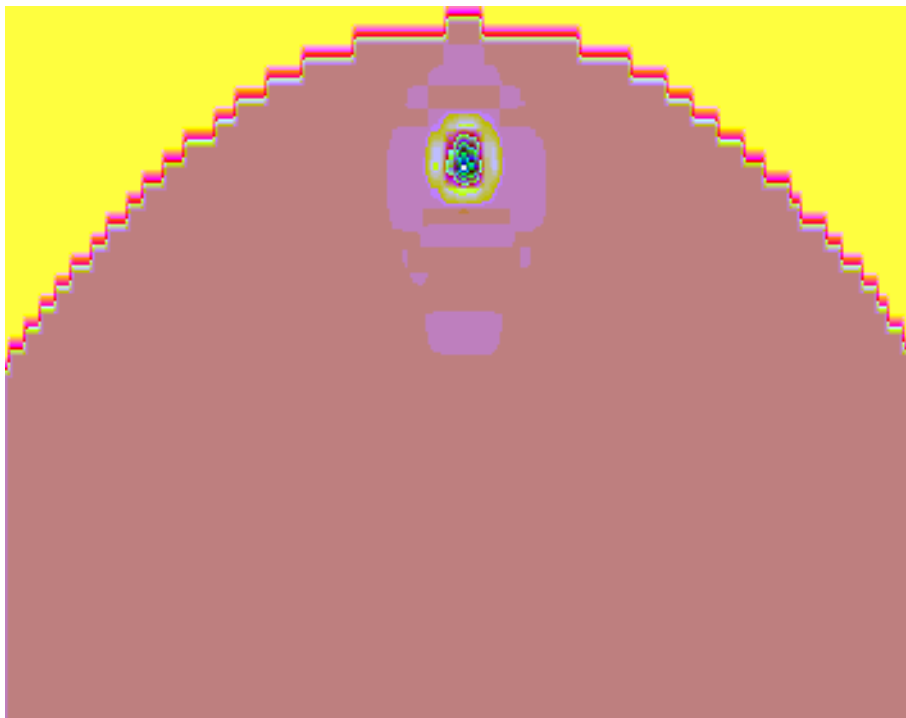
Figure 3. Excitation of a Ricker wavelet in a parabola's focal point. The vertical diagonal (from small ξ and κ to large ξ and κ) is shown.
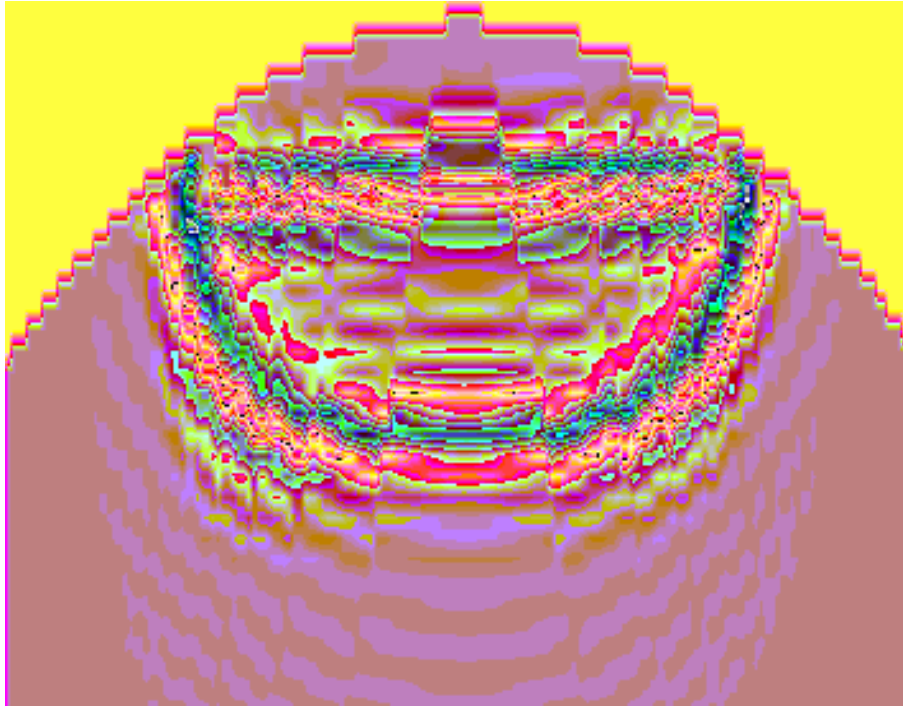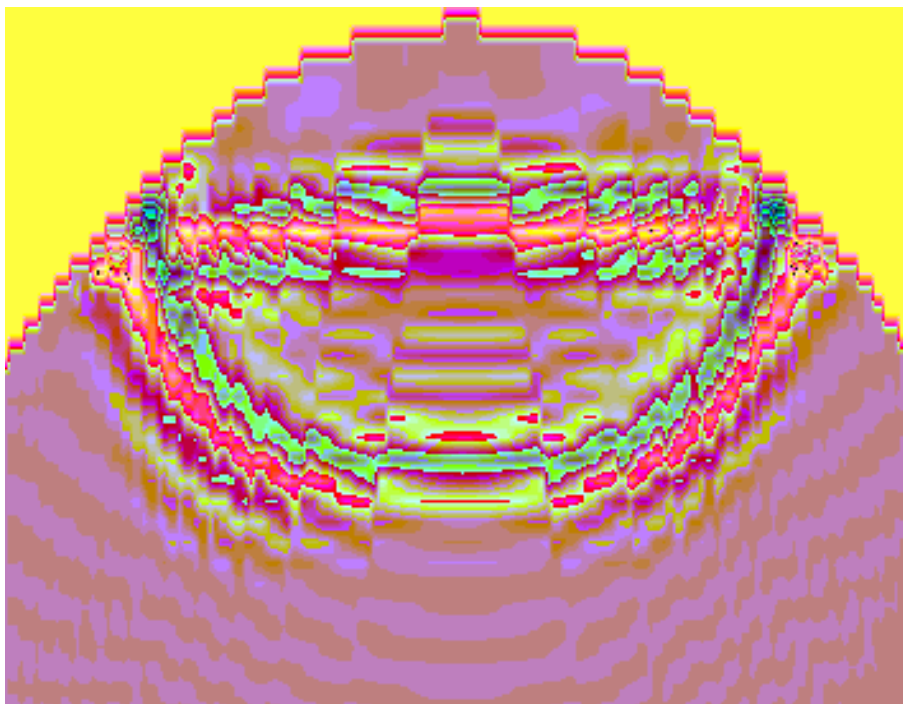
Figure 4. Reflected wave from the parabolic free surface ($t = 1.4$ s) in the elastic case. Diagonal vertical snapshot.

P velocity of 6 km s^{-1}, an S velocity of 3.46 km s^{-1} and a density of 2000 kg m^{-3}. The snapshots of Fig. 6 show the vertical particle velocity component of a viscoelastic simulation. Q is 250 for P and 200 for S waves.

At 1.5 s in Fig. 6 we see undisturbed P and Rg waves propagating away from the source point. After the P wave hits the trench, at 3.5 s we see a PR (P to Rg conversion) wave to the left of the trench behind the P wave in front of the Rg wave. By symmetry, this conversion can also be identified as a (more smoothed) reflection from the trench on its right side at this time, as well as a (similarly smoothed) PP reflection in front of it. The transmitted and reflected PR waves can be followed in the last two snapshots of Fig. 6, but here also transmitted and reflected RR waves can be traced behind them. I have confirmed that the

Figure 5. Reflected wave from the parabolic free surface ($t = 1.4$ s) in the viscoelastic case. Diagonal vertical snapshot.
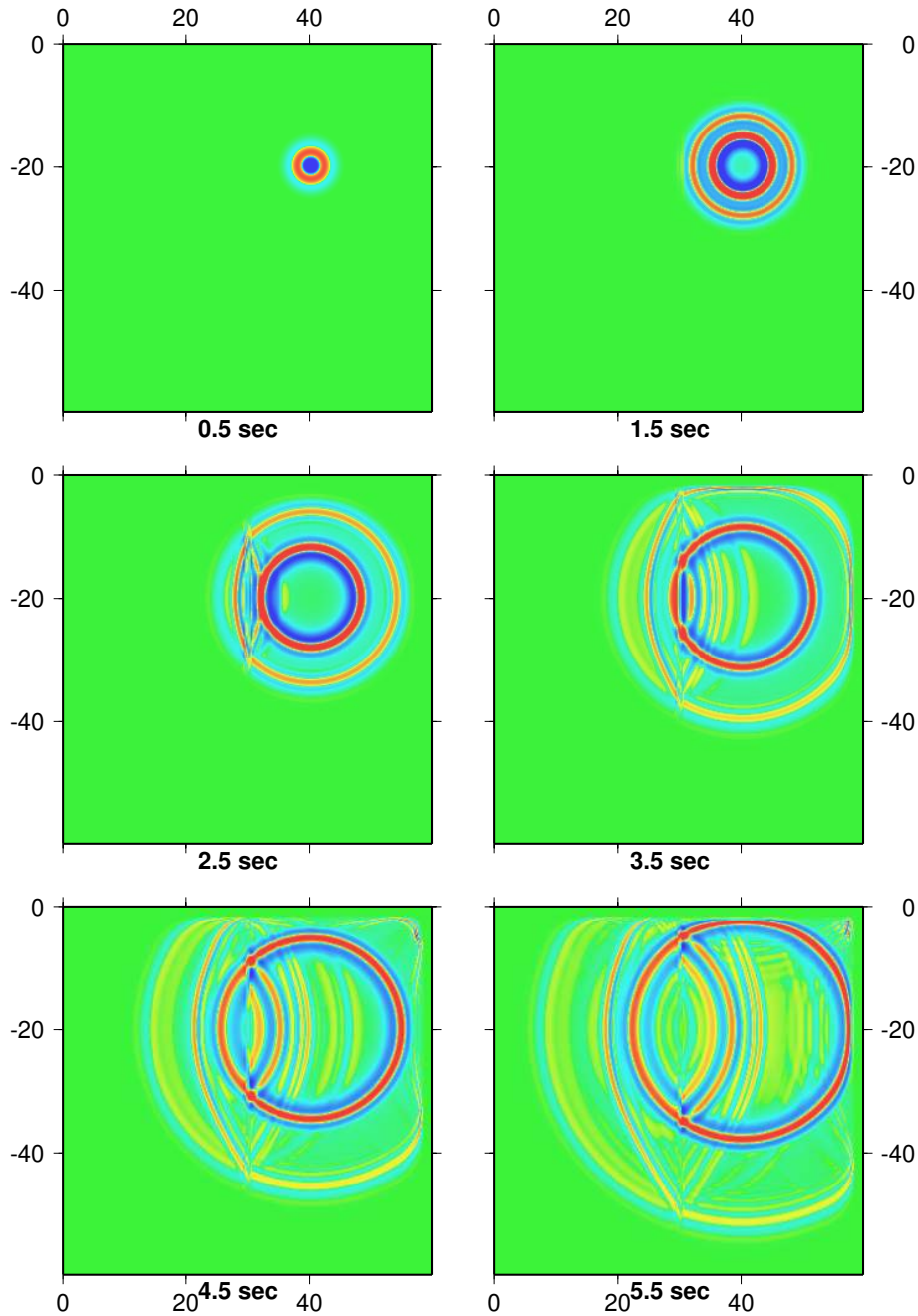
Figure 6. Snapshots of the vertical particle velocity component *w* at various times after a Ricker *P*-wave point source is released at the surface of a trench model. The 1.2 km deep and wide trench is oriented in the south–north direction in the middle of the domain. The snapshots of the viscoelastic simulation are taken along the surface topography.

amplitude of the *Rg* wave is weakened after transmission through the trench (Tessmer & Kosloff 1994) due to scattering.

Seismograms from the simulation are shown in Figs 7 and 8. I use the receiver locations of Fig. 9, which is a map covering a domain of the same size. This means that both the west–east- and the south–north-oriented sensor lines displayed contain the source at their middle positions. The stations cover lines of 30 km and have a spacing of 0.6 km. Fig. 7 is the vertical particle velocity component along the west–east-oriented line and clearly displays the original *P* and *Rg* waves as well as the reflected ones from the trench. The trench is located between receivers numbers 8 and 9. Because of scattering and the

effects of viscoelasticity, the reflected *Rg* waves appear as an attenuated, dispersed wave train. Fig. 8 shows the south–north-oriented receiver line. This line does not contain the trench and hence shows undistorted *P* and *Rg* waves for some time, until reflected *P* and *Rg* waves from the trench (*PP* and *PR*) hit the line in the last part of the seismogram. This is a real 3-D effect that will not occur in 2-D simulations. From Fig. 6 we see that *RR* reflections do not reach the line in the time simulated. Compared with the results of Tessmer & Kosloff (1994), we see that the present inclusion of viscoelasticity leads to some dispersed wave patterns in snapshots and seismograms of *RR* reflections and transmissions.

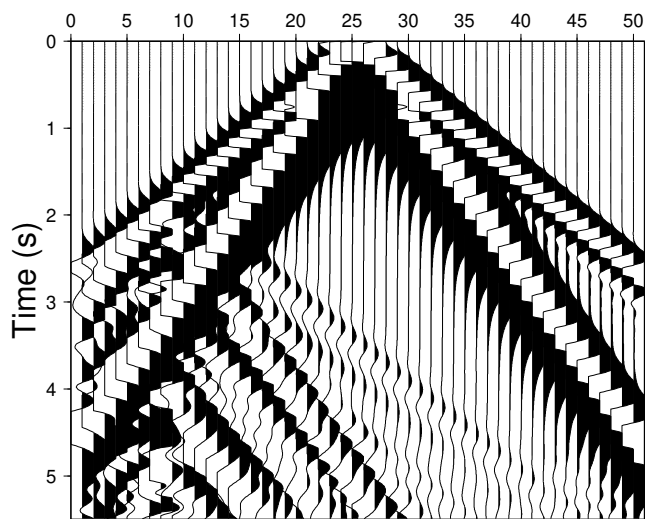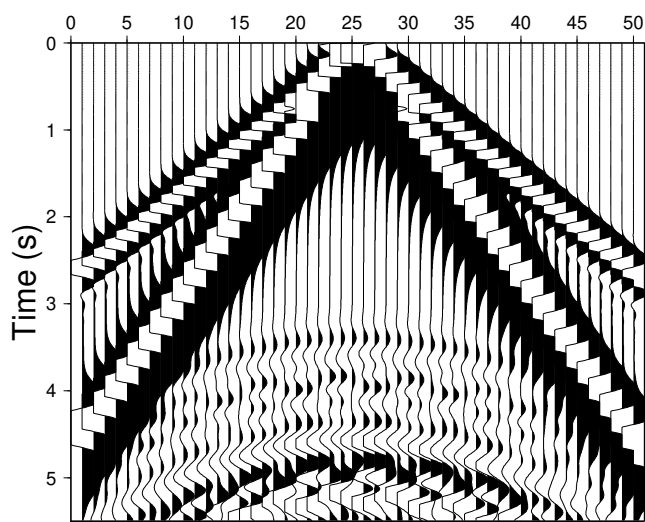## W, Viscoelastic, Trench, W-E profile

Figure 7. Seismogram of the vertical particle velocity component *w* of the viscoelastic simulation of Fig. 6 along the locations of the west–east-oriented receiver line of Fig. 9. The Ricker point *P* source is located at the middle point of the receiver line and the trench is located between receivers 8 and 9.

P TO RG SCATTERING FROM REAL TOPOGRAPHIC RELIEF

For the present 3-D FD simulations I have used digital elevation data from an area of 60×60 km containing the 3 km aperture NORESS array in southeastern Norway (Fig. 9). This hilly area was chosen because of easy access to detailed topographic data. Additionally, significant *P* to *Rg* scattering from

W, Viscoelastic, Trench, S-N profile

Figure 8. Seismogram of the vertical particle velocity component *w* of the viscoelastic simulation of Fig. 6 along the locations of the south–north-oriented receiver line of Fig. 9. The Ricker point *P* source is located at the middle point of the receiver line and the trench is parallel to the line and 10 km west of it.

© 1999 RAS, *GJI* **139,** 852–878

specific hills is well documented from NORESS record analysis (Bannister *et al.* 1990; Gupta *et al.* 1993; Hedlin *et al.* 1991; Hedlin *et al.* 1994). The most prominent topography present in the data set is the steep Skreikampen hill immediately west of the southern part of lake Mjøsa (the long south–north-oriented dark band in the southwest area of Fig. 9). In the first examples the source wave is a vertically incident plane *P* wave simulating a teleseismic short-period *P* phase. The centre frequency of the plane Ricker wavelet (point Ricker sources implemented along a plane) is 2.5 Hz, the *P* and *S* wave velocities of the homogeneous medium are 6.0 km s^{-1} and 3.46 km s^{-1} respectively and the density is 2000 kg m^{-3}. In all instances the given wave speeds are exact for the elastic case, that is, in the limit of infinite *Q* and/or zero frequency. I set $Q = 250$ for *P* waves and $Q = 200$ for *S* waves. I use a uniform grid sampling of 0.2 km and a total grid size of $300 \times 300 \times 100$. The viscoelastic simulation corresponds to a total computer memory of 1.4 GBytes using domain decomposition by Message Passing Interface (MPI) and took about 1 hr on 18 processors using the SGI (Cray) Origin 2000 parallel machine at the Department of Informatics, University of Bergen, Norway. The corresponding elastic simulation used a memory of slightly more than 1 GByte and took 15 min less on the same number of processors. Using domain decomposition parallelization via MPI on this machine enabled me to run 3-D models with about 10^8 gridpoints, as opposed to about 10^7 on earlier machines. The sizes of the present simulations are far below these maximum sizes.

The plane teleseismic *P* wave is vertically incident and released right below the topography surface. The first snapshot time of Figs 10 and 11 is $t = 0.5$ s and there is 1 s between each snapshot. The vertical sections of Fig. 10 are taken along the west–east topography profile (along the *xz*-plane) of Fig. 9. The left series shows the vertical particle velocity component *w* and the right series shows the horizontal particle velocity component *u*. Fig. 11 shows snapshots along the surface topography displaying the vertical particle velocity component *w*. Figs 12 and 13 are the same snapshots for the corresponding elastic case. An absorption thickness of 30 gridpoints is used along the grid boundaries in both the viscoelastic and the elastic cases, and exponential damping according to Cerjan *et al.* (1985) is used with an absorption constant of 0.05 in the elastic case. As expected, this case leads to artificial boundary reflections of stronger amplitudes than the viscoelastic case. I use a linear change of relaxation time over 20 gridpoints towards *Q*-values of 2.5 for *P* waves and 2.0 for *S* waves along the boundaries in strips of 10 gridpoints. This leads the strongest grid reflections in the viscoelastic case to be *Rg* waves propagating into the domain at a later stage than in the elastic case. The strong *Rg*-wave boundary reflections in the elastic case propagate into the domain much sooner. Although the exponential damping technique is the most efficient absorbing boundary method I have tested (Simone & Hestholm 1998), a wave incident at an angle of 90° to the boundary is the most difficult case. It is apparent that absorption layers of low *Q* along the grid boundaries in a viscoelastic scheme perform better than exponential damping in such a thin layer. Nevertheless, both cases generate clear grid boundary reflections. The reason is that the present situation of a plane wave reaching out to all grid edges is a worst-case scenario for grid reflection since wave components in every direction reach all grid edges along the surface immediately. Even so, I prefer to include these
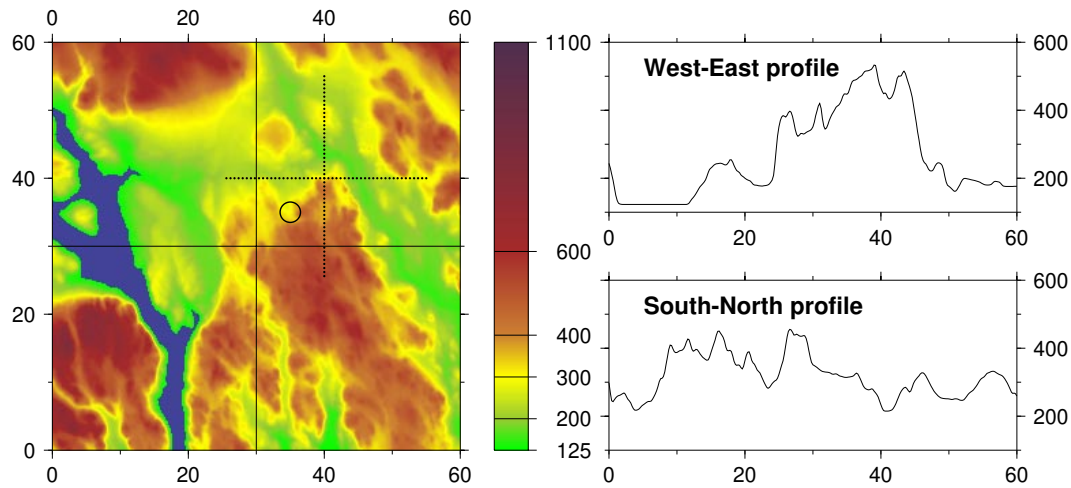
Figure 9. Left: map shows the topography of the 60×60 km area used in the 3-D simulations. The dashed lines show the positions of the receivers in two profiles and the circle outlines the NORESS array. Labels are in kilometres. The dark area to the southwest is Lake Mjøsa (123 m above sea level). Right: topography profiles along the two lines each of 60 km length shown on the map. They are midway along the *y*- and *x*-directions and cover respectively the complete *x*- and *y*-dimensions of the area. Horizontal axes are in kilometres and vertical axes are in metres above mean sea level.

examples both to show each wave modelling scheme's ability to absorb every incident wave component and to illustrate the behaviour of the topography boundary conditions at every location of the real topography as soon as possible. The viscoelastic grid reflections from the thin absorbing strips are clearly seen in Fig. 11 as straight lines, although the elastic grid reflections of Fig. 13 are more dominant and propagate into the domain sooner. Features of scattering can be seen in both cases, although the viscoelastic case gives more information due to later grid reflections.

Figs 11 and 13 show a circular wave pattern of *Rg* waves emanating from the area of prominent topography at 30 km from the south and 40 km from the west grid edges. The scattered surface waves appear to radiate out from secondary point sources that coincide with areas of high topographic gradients. This scattering originates from the steep valley side east of Bronkeberget about 10 km east of NORESS (Bannister *et al.* 1990). However, the surface wave with the highest amplitude in these examples is a slowly moving *Rg* wave propagating from the southwest corner of the area towards the centre of the domain. The steepest topography of the model can be found in this area close to Lake Mjøsa (the Skreikampen hill). *P*-to-*Rg* scattering in this area was observed by Bannister *et al.* (1990) and can now be realistically synthesized.

Using a simulation time of 5.5 s there is no noticeable difference between the viscoelastic and elastic cases for the present parameters. The *Q*-values (250 for *P* and 200 for *S* waves) are low used together with the high *P* velocity of 6 km s^{-1}. The applied centre frequency of 2.5 Hz then leads to such long wavelengths that there is no visible attenuation and dispersion of the wavefield for the times and scales shown. Using $A(x) = A_0 \exp\{-\pi f x/(cQ)\}$ (Aki & Richards 1980), where *f* is the central frequency, *c* is the wave speed, $A(x)$ is the wave amplitude at travel distance *x* and A_0 is the wave amplitude at travel distance 0, leads to attenuations of *Rg* waves of 10 per cent after 2.75 s and 20 per cent after 5.5 s of simulation time. This attenuation is unnoticeable in Fig. 11. In addition, from the dispersion curves in Robertsson *et al.* (1994), the present

parameters should lead to an approximate dispersion of 2 per cent, which after 5.5 s of simulation time of *Rg* waves corresponds to a maximum dispersion distance of 0.37 km. It is clear that these quantities are unnoticeable at the present scales and parameters, and so the scattering will look the same for the elastic and the viscoelastic cases. Therefore, the predominant argument for viscoelastic rather than elastic modelling for teleseismic distances and earthquake simulations is clearly the improved absorbing boundary conditions along the grid edges. Only six shades are used in Figs 10–13, therefore the small numerical dispersion in front of the wave fronts is magnified unrealistically in Figs 10 and 12. However, the displays show some of the *Rg* wave scattering very clearly.

I also show some seismograms from the simulations taken along the receiver profiles of Fig. 9. Fig. 14 is the second horizontal particle velocity component *v* from the viscoelastic simulation displayed along the west–east-oriented receiver profile of Fig. 9. The seismogram shows scattering from the topography, but after 3 s of simulation time boundary reflections from the northern grid boundary tend to dominate.

Figs 15 and 16 show the vertical particle velocity component *w* along the south–north-oriented receiver profile of Fig. 9 of the viscoelastic and elastic simulations respectively. Here the earlier and stronger boundary reflections in the elastic case are obvious, and we see clear irregular and very localized scattering from the surface topography. In the corresponding seismogram in the viscoelastic case of the first horizontal particle velocity component *u* (Fig. 17), the scattering exhibits a broader pattern and a stronger coherence affecting many more receivers at a time. This is expected since *Rg* waves travel predominantly horizontally along the surface. However, grid reflections from the eastern boundary dominate after 3 s of simulation time. Since the medium is homogeneous, the scattering we see is only due to the 3-D topography. Previous work (Hestholm *et al.* 1999) has shown that a great amount of scattering is due to out-of-plane effects from 3-D topography, as 2-D synthetics lead to much simpler seismograms.
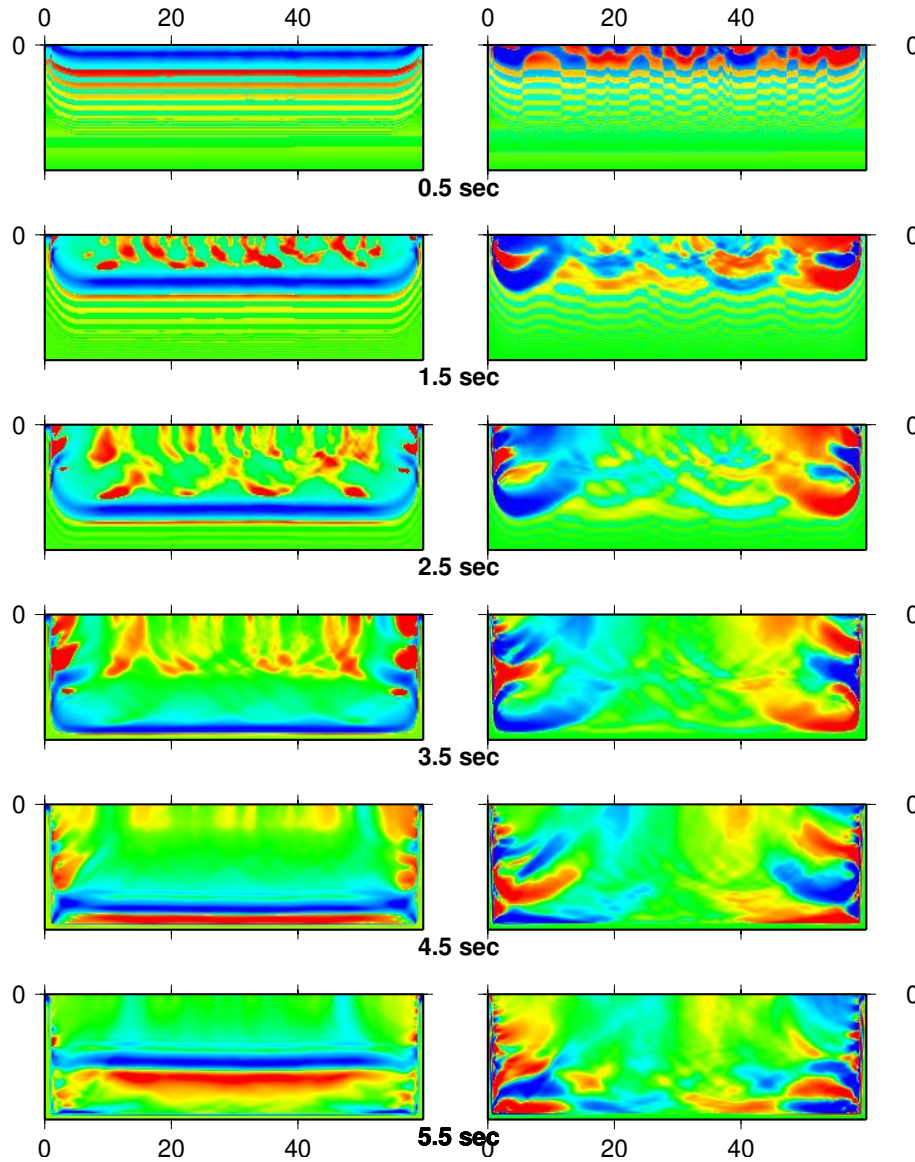
Figure 10. Snapshots of the vertical particle velocity component *w* (left series) and the first horizontal particle velocity component *u* (right series) at various times after a plane wave is released close to the surface topography of Fig. 9. The snapshots of the viscoelastic simulation are taken along the west–east topography profile of Fig. 9.

In the final example I show a viscoelastic simulation using an incident plane wave dipping towards the same surface topography area using the same grid parameters and dimensions and the same homogeneous medium as before. The example is included to represent an incoming wave from an earthquake or a teleseismic explosion in a more realistic way than in the last example. Snapshots along the vertical *xz*-plane of the *w* particle velocity component (left series) and the *u* particle velocity component (right series) are displayed in Fig. 18. Snapshots along the surface topography of the vertical (*w*) particle velocity component are shown in Fig. 19. The plane wave has the same small negative dip in both the *x*- and *y*-directions. This case leads to fewer grid boundary reflections than in the case of the vertically incident plane wave. We see that the same areas as before, that is, the area 30 km from the southern and 40 km from the western grid edges as well as the area near the southwest corner, give rise to the most prominent topography

scattering. In this case, however, the scattering from the first of these areas has not reached as far as it did for the horizontal plane wave at the same times because in this case the plane wave was not initiated as close to the surface. On the other hand, the dipping plane wave gives rise to scattering of stronger amplitudes than for the vertically incident (horizontal) plane wave. The snapshots are scaled relative to each other, and the surface topography scattering of Fig. 19 appears clearer than before. In the last snapshots (at 5.5 s) the bottom grid boundary reflection reaches the surface and hence represents an unphysical effect.

Figs 18 and 19 are snapshots representing clear pictures of the *Rg* scattering and the propagation of the plane wave reflection. They are scaled relative to the previous snapshots of Figs 10–13 and exhibit stronger scattering amplitudes. This illustrates the significance for local earthquake damage of source incidence angles.
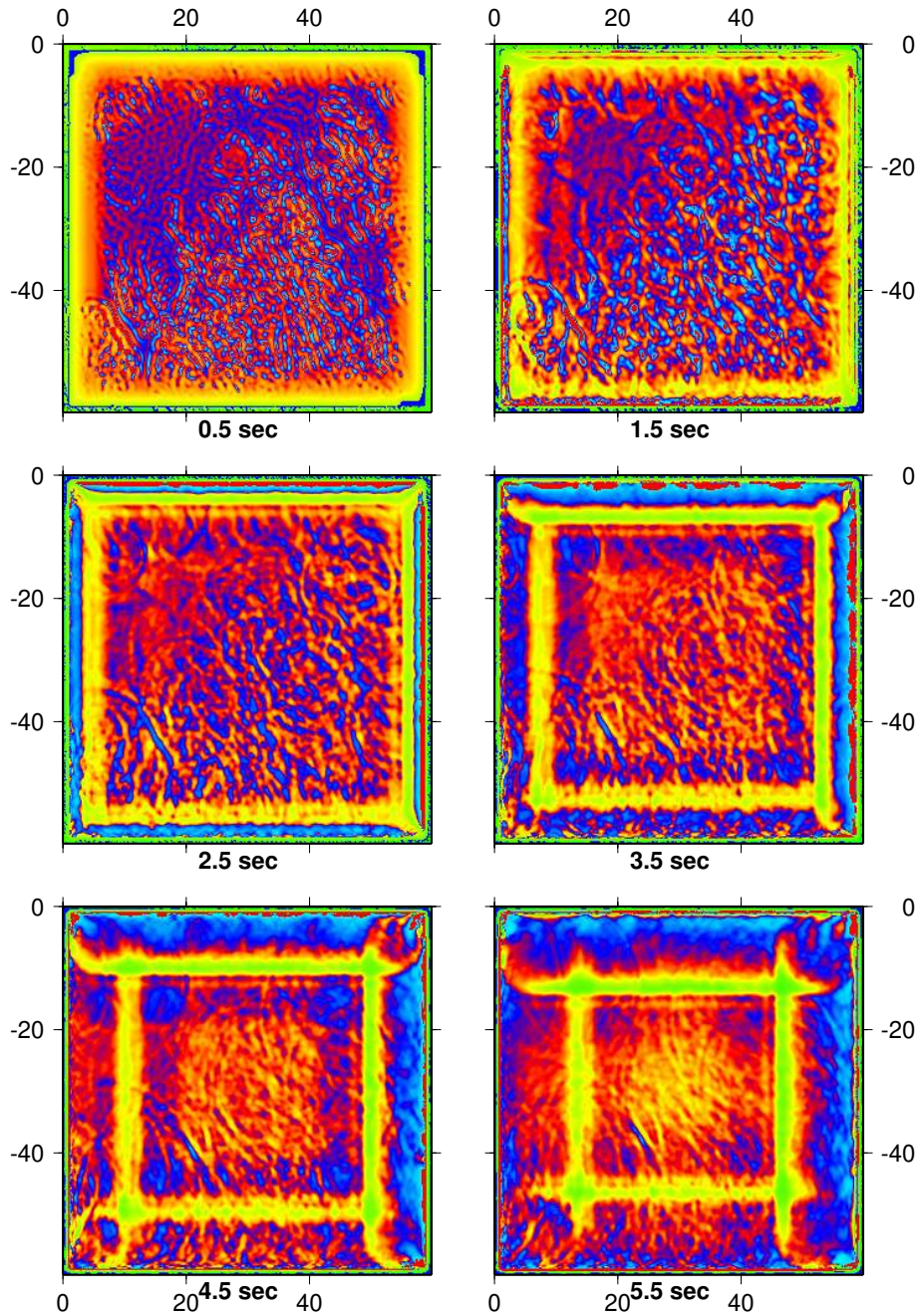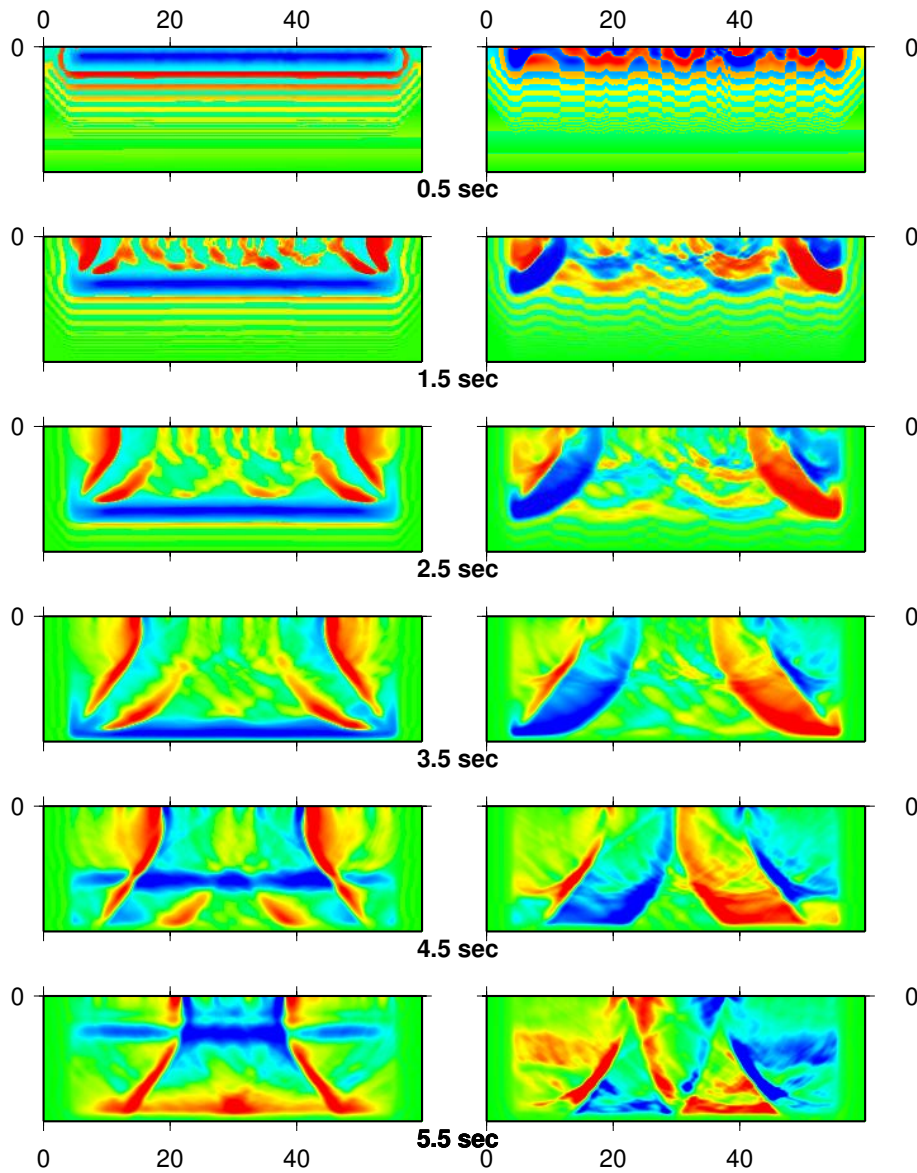
Figure 11. Snapshots of the vertical particle velocity component *w* at various times after a plane wave is released close to the surface topography of Fig. 9. The snapshots of the viscoelastic simulation are taken along the surface topography of Fig. 9.

Figs 20–22 are seismograms from the last simulation of the three particle velocity components *u*, *v* and *w* along the south–north-oriented receiver profile of Fig. 9. Apart from the plane wave reflection, these seismograms exhibit predominantly surface topography scattering. The horizontal velocity component scattering is more coherent than the *w* scattering, *u* more so than *v*.

DISCUSSION

In most land seismic profiling there is one or more low-velocity layers near the surface. 2-D investigations with the aim of quantifying the scattering from near-surface irregularities

have been performed (Hill & Levander 1984; Levander & Hill 1985). Irregularities were introduced laterally along the bottom boundary of a surface low-velocity layer. Comparing the results of a plane, vertically incident wave upon such a layer and upon a layer with a plane lower boundary, it is confirmed that energy of large-amplitude motion gets trapped near the free (plane) surface in the case of lateral corrugation of the lower boundary. The roughness induces a strong resonant coupling of incident *P* waves to *Rg* modes. Irregularities along the lower boundary are shown to cause the trapping of a large amount of energy in *Rg* modes near the free surface. This energy will stay strong and be the dominant feature of the wavefield after the main pulse has radiated out of the model. Similar results

Figure 12. Snapshots of the vertical particle velocity component *w* (left series) and the first horizontal particle velocity component *u* (right series) at various times after a plane wave is released close to the surface topography of Fig. 9. The snapshots of the elastic simulation are taken along the west–east topography profile of Fig. 9.

were obtained from a shallowly buried thin layer with random velocity perturbations. When such strong energy concentration along the free surface can be caused by irregularities along the bottom boundary of a low-velocity layer along the surface, one would think that irregularities along the much stronger dis-continuities of a free surface would cause even stronger energy trapping and conversions to *Rg* modes in the presence of such a low-velocity layer. These effects are not seen in the case of a plane surface and a homogeneous layer with smooth boundaries. In this case, energy escapes from the near-surface layer and is radiated back into the half-space after reverberation within the layer (Levander & Hill 1985). In the present work I show the effects of surface topographies without inclusion of near-surface low-velocity layers in order to attempt to isolate the effects of free-surface topography. 2-D FD elastic simulations with topography, random media perturbations of the crust and upper mantle and low-velocity layers near the free surface

have nevertheless been performed using the present method (Hestholm & Ruud 1994; Hestholm *et al.* 1994). An analysis of the results can be found in Ruud *et al.* (1993). Nonetheless, even in a homogeneous medium scattering from surface topography is quite effective, as is shown in this work.

A discussion of possible topography scattering in a data set assembled by Conoco in West Texas can be found in Imhof (1996). Although Imhof claimed (Chapter 6) that for records shot on top of the mesas, topography can be discarded as a major scattering mechanism because of the very smooth topo-graphy there, he mentioned that the record with the largest amount of 'noise' was the one shot across the roughest part of the mesa. To perform FD simulations with topography he used the method of Jih *et al.* (1988), resulting in relatively simple snapshots, although modelling of only incident *Rg* waves along the surface was performed. He attributed most of the scattering to near-surface cavities, but if simulations were to
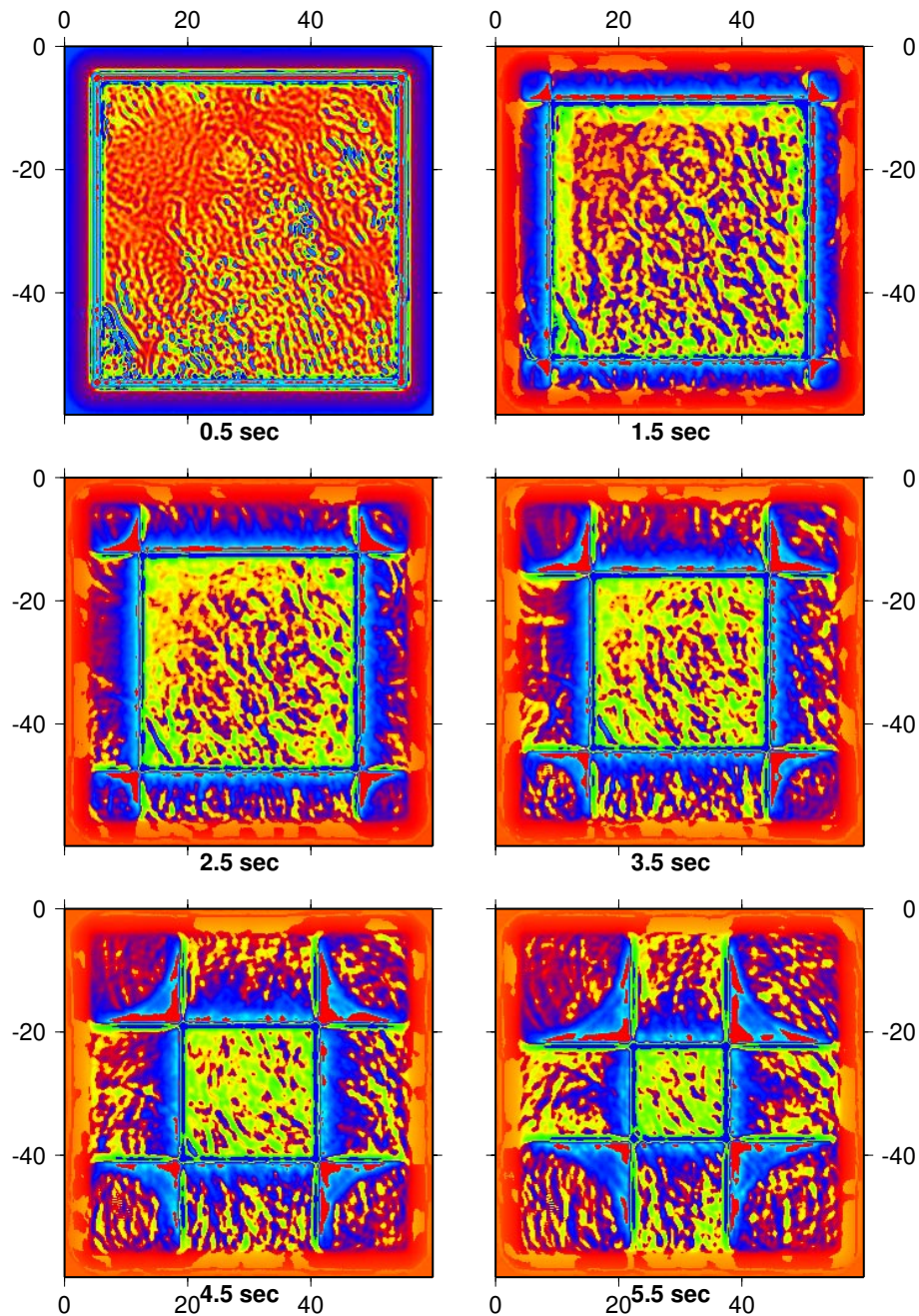
Figure 13. Snapshots of the vertical particle velocity component *w* at various times after a plane wave is released close to the surface topography of Fig. 9. The snapshots of the elastic simulation are taken along the surface topography of Fig. 9.

be done across the complete area of field data, including the debris-filled valleys, topography effects would surely be of great importance in the results.

Effects of topography are important for earthquake hazard assessment, and crustal studies have been pursued with this goal in mind using central frequencies of 1–10 Hz. The topography causes the amplitudes of seismic waves from earthquakes to vary significantly locally. The spectral content of the waves will accordingly be affected significantly by the topography (Pitarka & Irikura 1996). An FD algorithm for 'staircase' modelling of 3-D surface topography on top of an elastic medium is given in the work of Pitarka & Irikura (1996) and

used to model incident waves on simple topography structures and at the KOB–JMA site near Kobe, Japan. Low-frequency (1–3 Hz) amplification is attributed to local topography effects and high-frequency deamplification results from the deconstructive interference of scattered waves. The results agree well with ground motion recordings of aftershocks at the site. As already mentioned, Bouchon *et al.* (1996) used the boundary element method in the wavenumber domain and investigated the effect of a hill on the ground motion from an earthquake. The hill was cosine shaped with an elliptical base of ratio 2 : 1. Amplitude amplifications were consistently found to occur at and near the top of the hill over a broad range of frequencies.
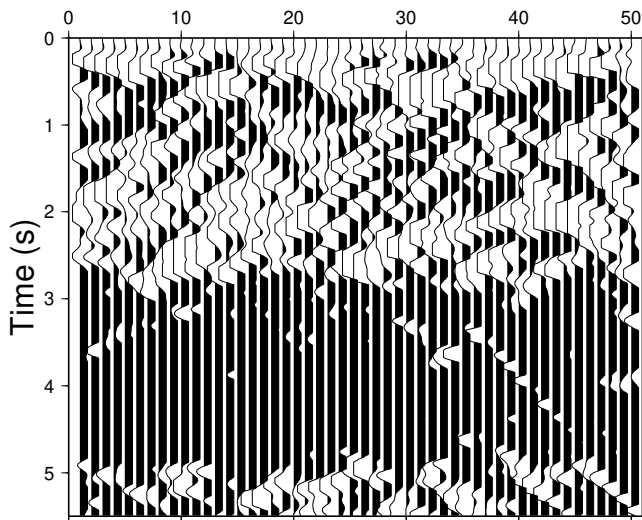
West - East Profile

Figure 14. Seismogram of the second horizontal particle velocity component *v* for the viscoelastic simulation of Figs 10 and 11 along the west–east-oriented receiver profile of Fig. 9.
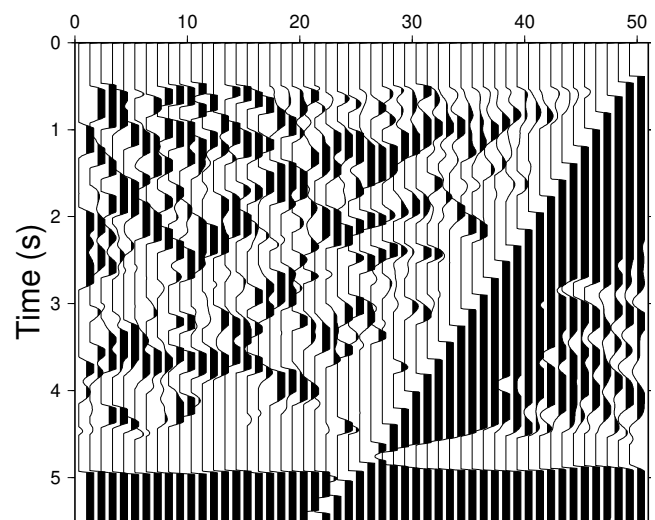
South - North Profile

Figure 16. Seismogram of the vertical particle velocity component *w* for the elastic simulation of Figs 12 and 13 along the south–north-oriented receiver profile of Fig. 9.

The results showed that amplifications are higher and stay higher over a much broader frequency band for incident shear waves polarized along the minor axis of the ellipse than for incident shear waves polarized along the longitudinal axis. A strong directivity of the scattered wavefield away from the topographic feature was also confirmed, exhibiting strong waves propagating along the minor axis of the ellipse, with almost no scattering along the longitudinal direction of the ellipse. This work is particularly interesting in that it assessed scattering effects (including frequency and directionality dependences) from a simple topographic structure for incident *S* waves with

different polarities. Theoretical and numerical results consistently predict amplification at topography ridge crests, but nevertheless almost always systematically underestimate actual amplifications observed in the field. Among the explanations for this is the 2-D nature of the topographic geometries assumed in calculations. Seismic responses from hills exhibit 3-D behaviour and there is a current lack of 3-D theoretical investigations.

Bannister *et al.* 1990) observed that some hills in the NORESS area literally radiate *Rg* waves at regular intervals for incident teleseismic waves of long durations. Array recordings are
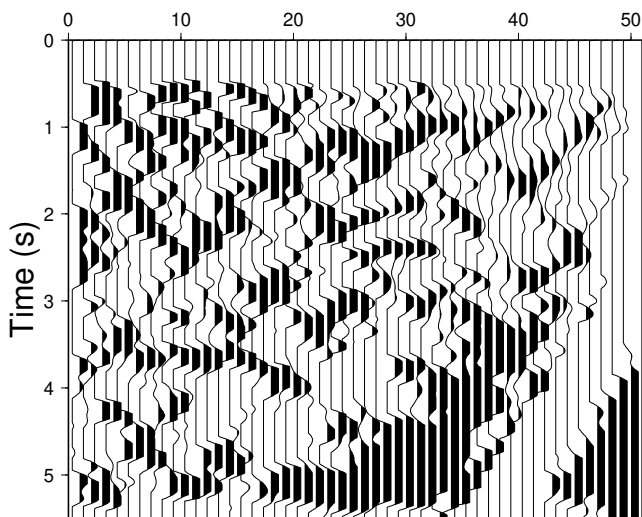
South - North Profile

Figure 15. Seismogram of the vertical particle velocity component *w* for the viscoelastic simulation of Figs 10 and 11 along the south–north-oriented receiver profile of Fig. 9.
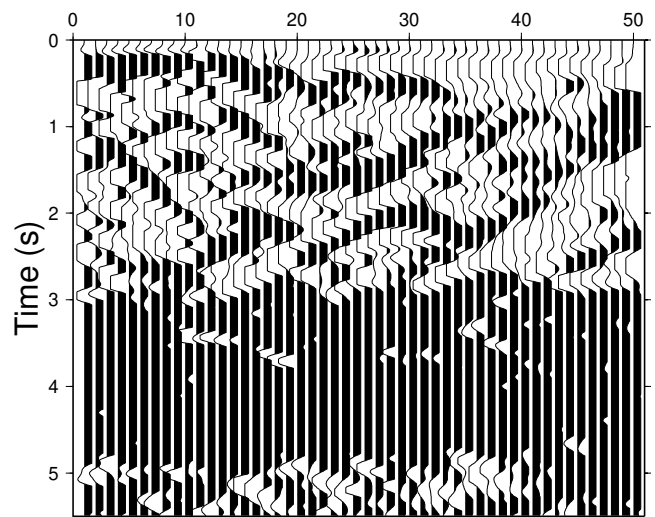
South - North Profile

Figure 17. Seismogram of the first horizontal particle velocity component *u* for the viscoelastic simulation of Figs 10 and 11 along the south–north-oriented receiver profile of Fig. 9.
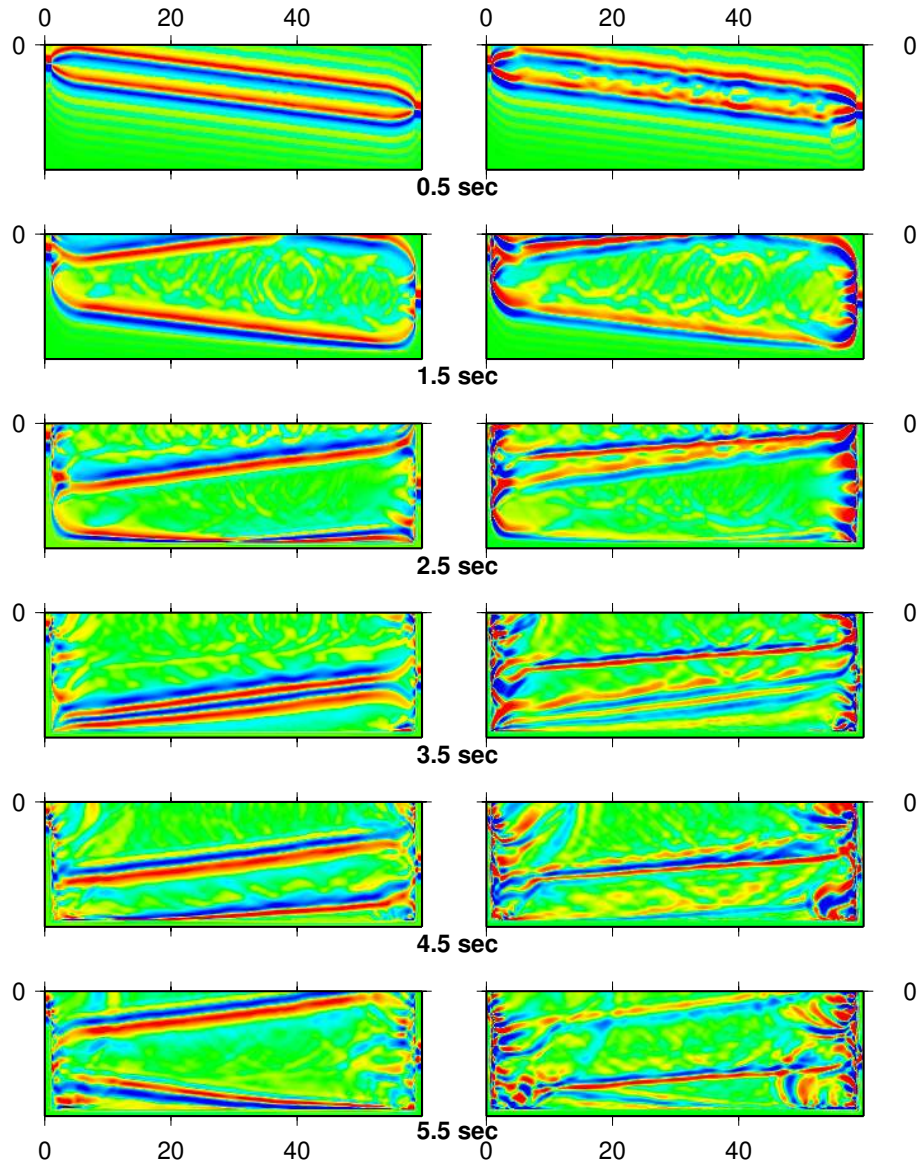
Figure 18. Snapshots of the vertical particle velocity component *w* (left series) and the first horizontal particle velocity component *u* (right series) at various times after a dipping plane wave is released near the surface topography of Fig. 9. The snapshots of the viscoelastic simulation are taken along the west–east topography profile of Fig. 9.

just point observations in this regard, whilst the synthetic snapshots in Figs 10–22 reveal nearly symmetric *Rg* radiation from such secondary sources. However, this radiation from a multiplicity of secondary sources becomes complex with time, so propagation directionality from a secondary source to a receiver can be very local and will also generally weaken with distance. Observationally this is confirmed by the fact that *Rg* waves rarely propagate further than 60 km in hilly areas such as those of the NORESS and GERESS (Bavaria, Germany) arrays, whilst across the plains of northern Fennoscandia *Rg* waves from explosions occasionally propagate out to 600 km.

CONCLUSIONS

Exact boundary conditions for free-surface topography combined with the viscoelastic wave equations in the velocity–

stress formulation give realistic scattering and complex wave patterns due to out-of-plane effects from 3-D topography. I have demonstrated clear *P*-to-*Rg* scattering from prominent topography and I find it gratifying that the strong *P*-to-*Rg* scattering from the Skreikampen and Bronkeberget hills observed by Bannister *et al.* (1990) through an analysis of NORESS recordings can be realistically synthesized. Another interesting phenomenon is that abrupt changes of the *Rg* wavefield occur over relatively small distances. This is due to the strong directivity of scattering from some topographic features as well as destructive interference from a multiplicity of secondary sources. Such wavefield characteristics are sometimes observed in recordings—at some sensors the *Rg* phase is prominent whilst it is hardly visible at nearby sensors less than 1 km away. Even in simulations of earthquakes and teleseismic explosions, where parameters close to elastic cases are used, it
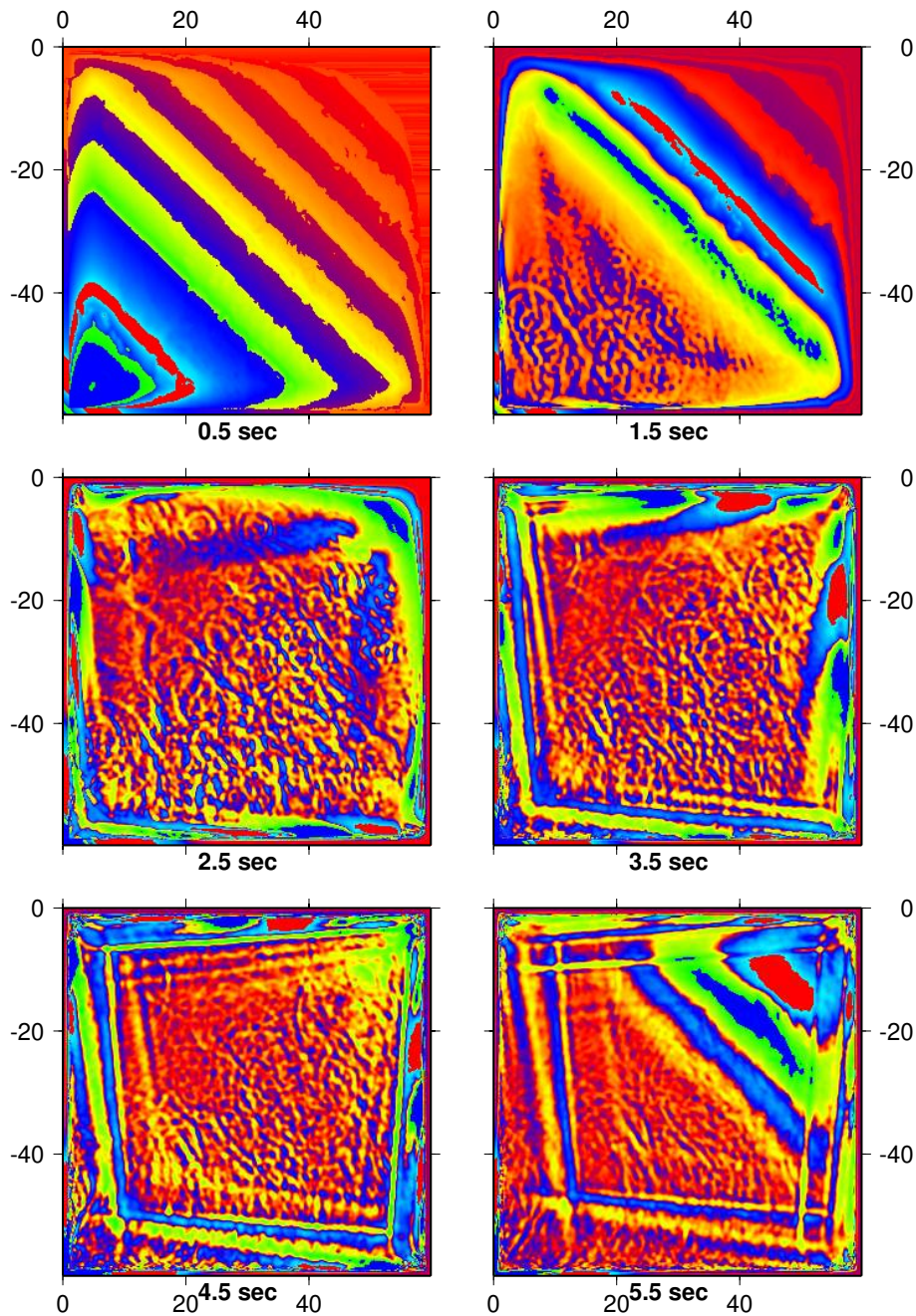
Figure 19. Snapshots of the vertical particle velocity component *w* at various times after a dipping plane wave is released near the surface topography of Fig. 9. The snapshots of the viscoelastic simulation are taken along the surface topography of Fig. 9.

is advantageous to use the viscoelastic code with a very high Q because of its superior absorbing boundary conditions along the grid edges. At longer time laps and/or lower Q-values it also gives realistic intrinsic attenuation and physical dispersion of all waves.
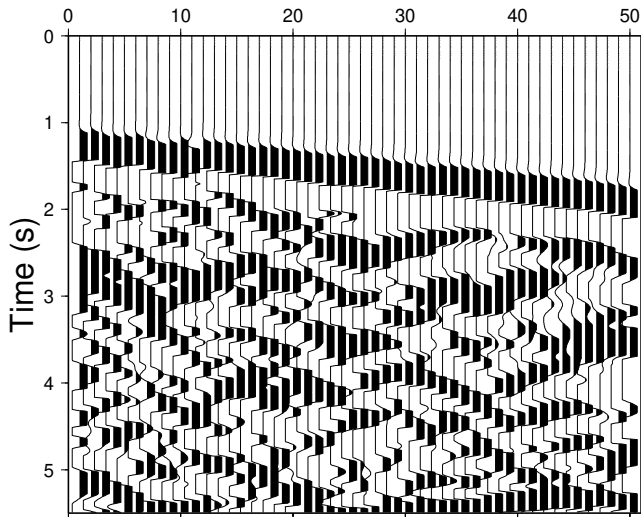
ACKNOWLEDGMENTS

South - North Profile

Figure 20. Seismogram of the first horizontal particle velocity component *u* for the viscoelastic simulation of Figs 18 and 19 along the south–north-oriented receiver profile of Fig. 9.
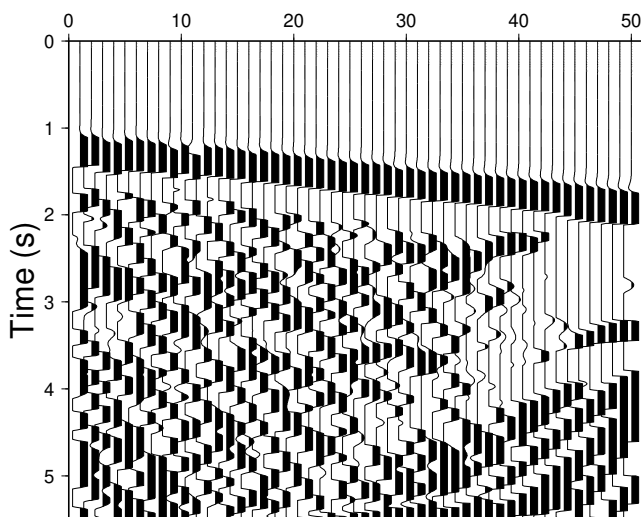
South - North Profile

Figure 21. Seismogram of the second horizontal particle velocity component *v* for the viscoelastic simulation of Figs 18 and 19 along the south–north-oriented receiver profile of Fig. 9.

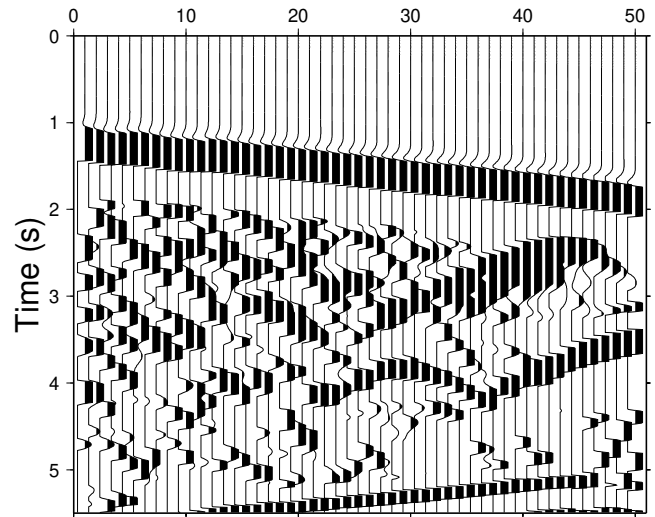## South - North Profile

Figure 22. Seismogram of the vertical particle velocity component *w* for the viscoelastic simulation of Figs 18 and 19 along the south–north-oriented receiver profile of Fig. 9.

REFERENCES

Aki, K. & Richards, P.G., 1980. *Quantitative Seismology, Theory and Methods,* Vol. I, W. H. Freeman, New York.

Bannister, S.C., Husebye, E.S. & Ruud, B.O., 1990. Teleseismic *P* coda analyzed by three-component and array techniques—deterministic location of topographic P-to-Rg scattering near the NORESS array, *Bull. seism. Soc. Am.,* **80,** 1969–1986.

Blanch, J.O., Robertsson, J.O.A. & Symes, W.W. 1995. Modeling of a constant Q: methodology and algorithm for an efficient and optimally inexpensive viscoelastic technique, *Geophysics,* **60,** 176–184.

Bouchon, M., Schultz, C.A. & Toksöz, M.N., 1996. Effect of three-dimensional topography on seismic motion, *J. geophys. Res.,* **101,** 5835–5846.

Carcione, J.M., 1993. Seismic modeling in viscoelastic media, *Geophysics,* **58,** 110–120.

Carcione, J.M., Kosloff, D. & Kosloff, R., 1988a. Wave propagation simulation in a linear viscoelastic medium, *Geophys. J. R. astr. Soc.,* **95,** 597–611.

Carcione, J.M., Kosloff, D. & Kosloff, R., 1988b. Wave propagation simulation in a linear viscoacoustic medium, *Geophys. J. R. astr. Soc.,* **93,** 393–407.

Cerjan, C., Kosloff, D., Kosloff, R. & Reshef, M., 1985. A non-reflecting boundary condition for discrete acoustic and elastic wave equations, *Geophysics,* **50,** 705–708.

Christensen, R.M., 1982. *Theory of Viscoelasticity—An Introduction,* Academic Press, San Diego.

Day, S.M. & Minster, J.B., 1984. Numerical simulation of attenuated wavefields using a Pade approximant method, *Geophys. J. R. astr. Soc.,* **78,** 105–118.

Fornberg, B., 1988a. Generation of finite difference formulas on arbitrary spaced grids, *Math. Comput.,* **51,** 699–706.

Fornberg, B., 1988b. The pseudospectral method: accurate representation of interfaces in elastic wave calculations, *Geophysics,* **53,** 625–637.

Frankel, A. & Leith, W., 1992. Evaluation of topographic effects on P and S-waves of explosions at the Northern Novaya Zemlya Test Site using 3-D numerical simulations, *Geophys. Res. Lett.,* **19,** 1887–1890.

Gupta, I.N., Lynnes, C.S. & Wagner, R.A., 1993. An array study of the effects of known local scatterers on regional phases, *Bull. seism. Soc. Am., 83,* 53–63.

Hedlin, M.A., Minster, J.B. & Orcutt, J.A., 1991. Beam-stack imaging using a small aperture array, *Geophys. Res. Lett., 18,* 1771–1774.

Hedlin, M.A., Minster, J.B. & Orcutt, J.A., 1994. Resolution of prominent crustal scatterers near the NORESS small-aperture array, *Geophys. J. Int., 119,* 101–115.

Hestholm, S.O. & Ruud, B.O., 1994. 2-D finite difference elastic wave modelling including surface topography, *Geophys. Prospect., 42,* 371–390.

Hestholm, S.O. & Ruud, B.O., 1998. 3-D finite difference elastic wave modeling including surface topography, *Geophysics, 63,* 613–622.

Hestholm, S.O., Husebye, E.S. & Ruud, B.O., 1994. Seismic wave propagation in complex crust–upper mantle media using 2-D finite-difference synthetics, *Geophys. J. Int., 118,* 643–670.

Hestholm, S.O., Ruud, B.O. & Husebye, E.S., 1999. 3-D versus 2-D finite difference seismic synthetics including real surface topography, *Phys. Earth planet. Inter., 113,* 339–354.

Hill, N.R. & Levander, A.R., 1984. Resonances of low-velocity layers with lateral variations, *Bull. seism. Soc. Am., 74,* 521–537.

Holberg, O., 1987. Computational aspects of the choice of operator and sampling interval of numerical differentiation in large-scale simulation of wave phenomena, *Geophys. Prospect., 35,* 629–655.

Imhof, M.G., 1996. Scattering of elastic waves using non-orthogonal expansions, *PhD thesis,* MIT, Cambridge, MA.

Jih, R.S., McLaughlin, K.L. & Der, Z.A., 1988. Free-boundary conditions of arbitrary topography in a two-dimensional explicit finite difference scheme, *Geophysics, 53,* 1045–1055.

Kindelan, M., Kamel, A. & Sguazzero, P., 1990. On the construction and efficiency of staggered numerical differentiators for the wave equation, *Geophysics, 55,* 107–110.

Komatitsch, M., Coutel, F. & Mora, P., 1996. Tensorial formulation of the wave equation for modelling curved interfaces, *Geophys. J. Int., 127,* 156–168.

Levander, A.R., 1988. Fourth-order finite-difference P–SV seismograms, *Geophysics, 53,* 1425–1436.

Levander, A.R. & Hill, N.R., 1985. P–SV resonances in irregular low-velocity surface layers, *Bull. seism. Soc. Am., 75,* 847–864.

Ohminato, T. & Chouet, B.A., 1997. A free-surface boundary condition for including 3D topography in the finite difference method, *Bull. seism. Soc. Am., 87,* 494–515.

Pitarka, A. & Irikura, K., 1996. Modeling 3-D surface topography by finite-difference method: Kobe-JMA station site, Japan, case study, *Geophys. Res. Lett., 23,* 2729–2732.

Robertsson, J.O.A., 1996. A numerical free-surface condition for elastic/viscoelastic finite-difference modeling in the presence of topography, *Geophysics, 61,* 1921–1934.

Robertsson, J.O.A., Blanch, J.O. & Symes, W.W., 1994. Viscoelastic finite-difference modeling, *Geophysics, 59,* 1444–1456.

Ruud, B.O., Husebye, E.S. & Hestholm, S.O., 1993. *Rg* observations from four continents: inverse- and forward-modelling experiments, *Geophys. J. Int., 114,* 465–472.

Sanchez-Sesma, F.J. & Campillo, M., 1991. Diffraction of P, SV, and Rayleigh waves by topographic features: a boundary integral formulation, *Bull. seism. Soc. Am., 81,* 2234–2253.

Sanchez-Sesma, F.J. & Luzon, F., 1995. Seismic response of three-dimensional alluvial valleys for incident P, S, and Rayleigh waves, *Bull. seism. Soc. Am., 85,* 269–284.

Simone, A. & Hestholm, S., 1998. Instabilities in applying absorbing boundary conditions to high order seismic modeling algorithms, *Geophysics, 63,* 1017–1023.

Sun, R. & McMechan, G.A., 1992. 2-D full-wavefield inversion for wide-aperture, elastic, seismic data, *Geophys. J. Int., 111,* 1–10.

Tal-Ezer, H., Carcione, J.M. & Kosloff, D., 1990. An accurate and efficient scheme for wave propagation in a linear viscoelastic medium, *Geophysics, 55,* 1366–1379.

Tessmer, E. & Kosloff, D., 1994. 3-D elastic modeling with surface topography by a Chebyshev spectral method, *Geophysics, 59,* 464–473.

Tessmer, E., Kosloff, D. & Behle, A., 1992. Elastic wave propagation simulation in the presence of surface topography, *Geophys. J. Int., 108,* 621–632.

Virieux, J., 1986. P-SV wave propagation in heterogeneous media: velocity–stress finite-difference method, *Geophysics, 51,* 889–901.

Xu, T. & McMechan, G.A., 1998. Efficient 3-D viscoelastic modeling with application to near-surface land seismic data, *Geophysics, 63,* 601–612.

APPENDIX A: FIRST-ORDER SYSTEM FROM THE CONSTITUTIVE RELATION

The constitutive relation for a linear viscoelastic isotropic homogeneous medium is (Christensen 1982)

$$\sigma_{ij} = \dot{\Lambda} * \delta_{ij}\varepsilon_{kk} + 2\dot{M} * \varepsilon_{ij}, \tag{A1}$$

where Einstein's summation convention is used. Λ and $2M$ are the two independent functions resulting from the fourth-order tensor G_{ijkl} in eq. (1) for a homogeneous medium. We define

$$\Pi = \Lambda + 2M \tag{A2}$$

and use the standard linear solid model for Π and M, i.e.

$$\Pi = \pi \left(1 - \sum_{\ell=1}^{L} \left(1 - \frac{\tau_{\varepsilon\ell}^{P}}{\tau_{\sigma\ell}} \right) e^{-t/\tau_{\sigma\ell}} \right) \theta(t), \tag{A3}$$

$$M = \mu \left(1 - \sum_{\ell=1}^{L} \left(1 - \frac{\tau_{\varepsilon\ell}^{S}}{\tau_{\sigma\ell}} \right) e^{-t/\tau_{\sigma\ell}} \right) \theta(t), \tag{A4}$$

where $\pi = \lambda + 2\mu$ and λ and μ are the elastic Lamé parameters. Π and M depend respectively on the strain relaxation time for P waves, $\tau_{\varepsilon\ell}^{P}$, and the strain relaxation time for S waves, $\tau_{\varepsilon\ell}^{S}$. This allows the independent definition of Q for P and S waves. Using the time derivative of the definition of strain,

$$\dot{\varepsilon}_{ij} = \frac{1}{2} \left(\partial_i v_j + \partial_j v_i \right), \tag{A5}$$

we obtain from the constitutive relation

$$\dot{\sigma}_{ii} = (\dot{\Pi} - 2\dot{M}) * \partial_k v_k + 2\dot{M} * \partial_i v_i \,, \tag{A6}$$

$$\dot{\sigma}_{ij} = \dot{M} * (\partial_i v_j + \partial_j v_i) \,, \quad i \neq j \,. \tag{A7}$$

Now we insert the standard linear solid expressions for Π and M and perform the time differentiation for each of their factors. We then obtain

$$\dot{\sigma}_{ii} = \left\{ \pi \left[1 - \sum_{\ell=1}^{L} \left(1 - \frac{\tau_{\varepsilon\ell}^P}{\tau_{\sigma\ell}} \right) \right] - 2\mu \left[1 - \sum_{\ell=1}^{L} \left(1 - \frac{\tau_{\varepsilon\ell}^S}{\tau_{\sigma\ell}} \right) \right] \right\} \partial_k v_k + 2\mu \left\{ 1 - \sum_{\ell=1}^{L} \left(1 - \frac{\tau_{\varepsilon\ell}^S}{\tau_{\sigma\ell}} \right) \right\} \partial_i v_i + \sum_{\ell=1}^{L} r_{ii\ell} \,, \tag{A8}$$

$$\dot{\sigma}_{ij} = \mu \left\{ 1 - \sum_{\ell=1}^{L} \left(1 - \frac{\tau_{\varepsilon\ell}^S}{\tau_{\sigma\ell}} \right) \right\} (\partial_i v_j + \partial_j v_i) + \sum_{\ell=1}^{L} r_{ij\ell} \,, \quad i \neq j \,, \tag{A9}$$

where

$$r_{ii\ell} = \left\{ \pi \frac{1}{\tau_{\sigma\ell}} \left(1 - \frac{\tau_{\varepsilon\ell}^P}{\tau_{\sigma\ell}} \right) - 2\mu \frac{1}{\tau_{\sigma\ell}} \left(1 - \frac{\tau_{\varepsilon\ell}^S}{\tau_{\sigma\ell}} \right) \right\} e^{-t/\tau_{\sigma\ell}} \theta(t) * \partial_k v_k + 2\mu \frac{1}{\tau_{\sigma\ell}} \left(1 - \frac{\tau_{\varepsilon\ell}^S}{\tau_{\sigma\ell}} \right) e^{-t/\tau_{\sigma\ell}} \theta(t) * \partial_i v_i \,, \quad 1 \leq \ell \leq L \,, \tag{A10}$$

$$r_{ij\ell} = \mu \frac{1}{\tau_{\sigma\ell}} \left(1 - \frac{\tau_{\varepsilon\ell}^S}{\tau_{\sigma\ell}} \right) e^{-t/\tau_{\sigma\ell}} \theta(t) * (\partial_i v_j + \partial_j v_i) \,, \quad i \neq j \,, \quad 1 \leq \ell \leq L \,. \tag{A11}$$

are the memory variables. We obtain the first-order system for them by evaluating the time derivatives the same way as was done in the previous step,

$$\dot{r}_{ii\ell} = -\frac{1}{\tau_{\sigma\ell}} \left\{ r_{ii\ell} + \left[\pi \left(\frac{\tau_{\varepsilon\ell}^P}{\tau_{\sigma\ell}} - 1 \right) - 2\mu \left(\frac{\tau_{\varepsilon\ell}^S}{\tau_{\sigma\ell}} - 1 \right) \right] \partial_k v_k + 2\mu \left(\frac{\tau_{\varepsilon\ell}^S}{\tau_{\sigma\ell}} - 1 \right) \partial_i v_i \right\} \,, \quad 1 \leq \ell \leq L \,, \tag{A12}$$

$$\dot{r}_{ij\ell} = -\frac{1}{\tau_{\sigma\ell}} \left\{ r_{ij\ell} + \mu \left(\frac{\tau_{\varepsilon\ell}^S}{\tau_{\sigma\ell}} - 1 \right) (\partial_i v_j + \partial_j v_i) \right\} \,, \quad i \neq j \,, \quad 1 \leq \ell \leq L \,. \tag{A13}$$

The momentum conservation equation completes the viscoelastic wave equations,

$$\rho \dot{v}_i = \partial_j \sigma_{ij} + \mathbf{f}_i \,, \tag{A14}$$

where $\mathbf{f}_i$ is the volume force and ρ is the density. The 3-D case for $L = 1$ (one standard linear solid) yields eqs (3)–(17).

APPENDIX B: PARTIAL DERIVATIVES IN MEDIUM EQUATIONS

For the medium equations we need $\partial\eta/\partial x$, $\partial\eta/\partial y$ and $\partial\eta/\partial z$. They are found from

$$\frac{\partial x}{\partial \xi} \frac{\partial \xi}{\partial x} + \frac{\partial x}{\partial \kappa} \frac{\partial \kappa}{\partial x} + \frac{\partial x}{\partial \eta} \frac{\partial \eta}{\partial x} = 1 \,, \tag{B1}$$

$$\frac{\partial y}{\partial \xi} \frac{\partial \xi}{\partial x} + \frac{\partial y}{\partial \kappa} \frac{\partial \kappa}{\partial x} + \frac{\partial y}{\partial \eta} \frac{\partial \eta}{\partial x} = 0 \,, \tag{B2}$$

$$\frac{\partial z}{\partial \xi} \frac{\partial \xi}{\partial x} + \frac{\partial z}{\partial \kappa} \frac{\partial \kappa}{\partial x} + \frac{\partial z}{\partial \eta} \frac{\partial \eta}{\partial x} = 0 \,, \tag{B3}$$

$$\frac{\partial x}{\partial \xi} \frac{\partial \xi}{\partial y} + \frac{\partial x}{\partial \kappa} \frac{\partial \kappa}{\partial y} + \frac{\partial x}{\partial \eta} \frac{\partial \eta}{\partial y} = 0 \,, \tag{B4}$$

$$\frac{\partial y}{\partial \xi} \frac{\partial \xi}{\partial y} + \frac{\partial y}{\partial \kappa} \frac{\partial \kappa}{\partial y} + \frac{\partial y}{\partial \eta} \frac{\partial \eta}{\partial y} = 1 \,, \tag{B5}$$

$$\frac{\partial z}{\partial \xi} \frac{\partial \xi}{\partial y} + \frac{\partial z}{\partial \kappa} \frac{\partial \kappa}{\partial y} + \frac{\partial z}{\partial \eta} \frac{\partial \eta}{\partial y} = 0 \,, \tag{B6}$$

$$\frac{\partial x}{\partial \xi} \frac{\partial \xi}{\partial z} + \frac{\partial x}{\partial \kappa} \frac{\partial \kappa}{\partial z} + \frac{\partial x}{\partial \eta} \frac{\partial \eta}{\partial z} = 0 \,, \tag{B7}$$

$$\frac{\partial y}{\partial \xi} \frac{\partial \xi}{\partial z} + \frac{\partial y}{\partial \kappa} \frac{\partial \kappa}{\partial z} + \frac{\partial y}{\partial \eta} \frac{\partial \eta}{\partial z} = 0 \,, \tag{B8}$$

$$\frac{\partial z}{\partial \xi} \frac{\partial \xi}{\partial z} + \frac{\partial z}{\partial \kappa} \frac{\partial \kappa}{\partial z} + \frac{\partial z}{\partial \eta} \frac{\partial \eta}{\partial z} = 1 \,. \tag{B9}$$

This leads to

$$\frac{\partial \eta}{\partial x} = \left(\frac{\partial y}{\partial \xi} \frac{\partial z}{\partial \kappa} - \frac{\partial z}{\partial \xi} \frac{\partial y}{\partial \kappa} \right) \bigg/ J , \tag{B10}$$

$$\frac{\partial \eta}{\partial y} = \left(\frac{\partial z}{\partial \xi} \frac{\partial x}{\partial \kappa} - \frac{\partial x}{\partial \xi} \frac{\partial z}{\partial \kappa} \right) \bigg/ J , \tag{B11}$$

$$\frac{\partial \eta}{\partial z} = \left(\frac{\partial x}{\partial \xi} \frac{\partial y}{\partial \kappa} - \frac{\partial y}{\partial \xi} \frac{\partial x}{\partial \kappa} \right) \bigg/ J , \tag{B12}$$

where

$$J = \frac{\partial x}{\partial \xi} \left(\frac{\partial y}{\partial \kappa} \frac{\partial z}{\partial \eta} - \frac{\partial z}{\partial \kappa} \frac{\partial y}{\partial \eta} \right) - \frac{\partial x}{\partial \kappa} \left(\frac{\partial y}{\partial \xi} \frac{\partial z}{\partial \eta} - \frac{\partial y}{\partial \eta} \frac{\partial z}{\partial \xi} \right) + \frac{\partial x}{\partial \eta} \left(\frac{\partial y}{\partial \xi} \frac{\partial z}{\partial \kappa} - \frac{\partial z}{\partial \xi} \frac{\partial y}{\partial \kappa} \right) . \tag{B13}$$

With our choice of mapping functions, eqs (18)–(20), we obtain

$$\frac{\partial x}{\partial \xi} = 1 , \qquad \frac{\partial x}{\partial \kappa} = 0 , \qquad \frac{\partial x}{\partial \eta} = 0 , \tag{B14}$$

$$\frac{\partial y}{\partial \xi} = 0 , \qquad \frac{\partial y}{\partial \kappa} = 1 , \qquad \frac{\partial y}{\partial \eta} = 0 , \tag{B15}$$

$$\frac{\partial z}{\partial \xi} = \frac{\eta}{\eta_{\max}} \frac{\partial z_0(\xi, \kappa)}{\partial \xi} , \qquad \frac{\partial z}{\partial \kappa} = \frac{\eta}{\eta_{\max}} \frac{\partial z_0(\xi, \kappa)}{\partial \kappa} , \qquad \frac{\partial z}{\partial \eta} = \frac{z_0(\xi, \kappa)}{\eta_{\max}} \tag{B16}$$

and

$$J = \frac{\partial z}{\partial \eta} = \frac{z_0(\xi, \kappa)}{\eta_{\max}} . \tag{B17}$$

From this we obtain expressions (24)–(28).

APPENDIX C: MEDIUM EQUATIONS

Applying the chain rule to eqs (3)–(17) and using the properties of eqs (21)–(23) leads to

$$\rho \frac{\partial u}{\partial t} = \frac{\partial \sigma_{xx}}{\partial \xi} + \frac{\partial \sigma_{xx}}{\partial \eta} \frac{\partial \eta}{\partial x} + \frac{\partial \sigma_{xy}}{\partial \kappa} + \frac{\partial \sigma_{xy}}{\partial \eta} \frac{\partial \eta}{\partial y} + \frac{\partial \sigma_{xz}}{\partial \eta} \frac{\partial \eta}{\partial z} + f_x , \tag{C1}$$

$$\rho \frac{\partial v}{\partial t} = \frac{\partial \sigma_{xy}}{\partial \xi} + \frac{\partial \sigma_{xy}}{\partial \eta} \frac{\partial \eta}{\partial x} + \frac{\partial \sigma_{yy}}{\partial \kappa} + \frac{\partial \sigma_{yy}}{\partial \eta} \frac{\partial \eta}{\partial y} + \frac{\partial \sigma_{yz}}{\partial \eta} \frac{\partial \eta}{\partial z} + f_y , \tag{C2}$$

$$\rho \frac{\partial w}{\partial t} = \frac{\partial \sigma_{xz}}{\partial \xi} + \frac{\partial \sigma_{xz}}{\partial \eta} \frac{\partial \eta}{\partial x} + \frac{\partial \sigma_{yz}}{\partial \kappa} + \frac{\partial \sigma_{yz}}{\partial \eta} \frac{\partial \eta}{\partial y} + \frac{\partial \sigma_{zz}}{\partial \eta} \frac{\partial \eta}{\partial z} + f_z , \tag{C3}$$

$$\frac{\partial \sigma_{xx}}{\partial t} = \pi \frac{\tau_\varepsilon^P}{\tau_\sigma} \left(\frac{\partial u}{\partial \xi} + \frac{\partial u}{\partial \eta} \frac{\partial \eta}{\partial x} + \frac{\partial v}{\partial \kappa} + \frac{\partial v}{\partial \eta} \frac{\partial \eta}{\partial y} + \frac{\partial w}{\partial \eta} \frac{\partial \eta}{\partial z} \right) - 2\mu \frac{\tau_\varepsilon^S}{\tau_\sigma} \left(\frac{\partial v}{\partial \kappa} + \frac{\partial v}{\partial \eta} \frac{\partial \eta}{\partial y} + \frac{\partial w}{\partial \eta} \frac{\partial \eta}{\partial z} \right) + r_{xx} , \tag{C4}$$

$$\frac{\partial \sigma_{yy}}{\partial t} = \pi \frac{\tau_\varepsilon^P}{\tau_\sigma} \left(\frac{\partial u}{\partial \xi} + \frac{\partial u}{\partial \eta} \frac{\partial \eta}{\partial x} + \frac{\partial v}{\partial \kappa} + \frac{\partial v}{\partial \eta} \frac{\partial \eta}{\partial y} + \frac{\partial w}{\partial \eta} \frac{\partial \eta}{\partial z} \right) - 2\mu \frac{\tau_\varepsilon^S}{\tau_\sigma} \left(\frac{\partial u}{\partial \xi} + \frac{\partial u}{\partial \eta} \frac{\partial \eta}{\partial x} + \frac{\partial w}{\partial \eta} \frac{\partial \eta}{\partial z} \right) + r_{yy} , \tag{C5}$$

$$\frac{\partial \sigma_{zz}}{\partial t} = \pi \frac{\tau_\varepsilon^P}{\tau_\sigma} \left(\frac{\partial u}{\partial \xi} + \frac{\partial u}{\partial \eta} \frac{\partial \eta}{\partial x} + \frac{\partial v}{\partial \kappa} + \frac{\partial v}{\partial \eta} \frac{\partial \eta}{\partial y} + \frac{\partial w}{\partial \eta} \frac{\partial \eta}{\partial z} \right) - 2\mu \frac{\tau_\varepsilon^S}{\tau_\sigma} \left(\frac{\partial u}{\partial \xi} + \frac{\partial u}{\partial \eta} \frac{\partial \eta}{\partial x} + \frac{\partial v}{\partial \kappa} + \frac{\partial v}{\partial \eta} \frac{\partial \eta}{\partial y} \right) + r_{zz} , \tag{C6}$$

$$\frac{\partial \sigma_{xy}}{\partial t} = \mu \frac{\tau_\varepsilon^S}{\tau_\sigma} \left(\frac{\partial u}{\partial \kappa} + \frac{\partial u}{\partial \eta} \frac{\partial \eta}{\partial y} + \frac{\partial v}{\partial \xi} + \frac{\partial v}{\partial \eta} \frac{\partial \eta}{\partial x} \right) + r_{xy} , \tag{C7}$$

$$\frac{\partial \sigma_{xz}}{\partial t} = \mu \frac{\tau_\varepsilon^S}{\tau_\sigma} \left(\frac{\partial u}{\partial \eta} \frac{\partial \eta}{\partial z} + \frac{\partial w}{\partial \xi} + \frac{\partial w}{\partial \eta} \frac{\partial \eta}{\partial x} \right) + r_{xz} , \tag{C8}$$

$$\frac{\partial \sigma_{yz}}{\partial t} = \mu \frac{\tau_\varepsilon^S}{\tau_\sigma} \left(\frac{\partial v}{\partial \eta} \frac{\partial \eta}{\partial z} + \frac{\partial w}{\partial \kappa} + \frac{\partial w}{\partial \eta} \frac{\partial \eta}{\partial y} \right) + r_{yz} , \tag{C9}$$

$$\frac{\partial r_{xx}}{\partial t} = -\frac{1}{\tau_\sigma} \left\{ r_{xx} + \pi \left(\frac{\tau_\varepsilon^P}{\tau_\sigma} - 1 \right) \left(\frac{\partial u}{\partial \xi} + \frac{\partial u}{\partial \eta} \frac{\partial \eta}{\partial x} + \frac{\partial v}{\partial \kappa} + \frac{\partial v}{\partial \eta} \frac{\partial \eta}{\partial y} + \frac{\partial w}{\partial \eta} \frac{\partial \eta}{\partial z} \right) - 2\mu \left(\frac{\tau_\varepsilon^S}{\tau_\sigma} - 1 \right) \left(\frac{\partial v}{\partial \kappa} + \frac{\partial v}{\partial \eta} \frac{\partial \eta}{\partial y} + \frac{\partial w}{\partial \eta} \frac{\partial \eta}{\partial z} \right) \right\} , \tag{C10}$$

$$\frac{\partial r_{yy}}{\partial t} = -\frac{1}{\tau_\sigma}\left\{ r_{yy} + \pi\left(\frac{\tau_\varepsilon^P}{\tau_\sigma}-1\right)\left(\frac{\partial u}{\partial \xi}+\frac{\partial u}{\partial \eta}\frac{\partial \eta}{\partial x}+\frac{\partial v}{\partial \kappa}+\frac{\partial v}{\partial \eta}\frac{\partial \eta}{\partial y}+\frac{\partial w}{\partial \eta}\frac{\partial \eta}{\partial z}\right) - 2\mu\left(\frac{\tau_\varepsilon^S}{\tau_\sigma}-1\right)\left(\frac{\partial u}{\partial \xi}+\frac{\partial u}{\partial \eta}\frac{\partial \eta}{\partial x}+\frac{\partial w}{\partial \eta}\frac{\partial \eta}{\partial z}\right)\right\}, \tag{C11}$$

$$\frac{\partial r_{zz}}{\partial t} = -\frac{1}{\tau_\sigma}\left\{ r_{zz} + \pi\left(\frac{\tau_\varepsilon^P}{\tau_\sigma}-1\right)\left(\frac{\partial u}{\partial \xi}+\frac{\partial u}{\partial \eta}\frac{\partial \eta}{\partial x}+\frac{\partial v}{\partial \kappa}+\frac{\partial v}{\partial \eta}\frac{\partial \eta}{\partial y}+\frac{\partial w}{\partial \eta}\frac{\partial \eta}{\partial z}\right) - 2\mu\left(\frac{\tau_\varepsilon^S}{\tau_\sigma}-1\right)\left(\frac{\partial u}{\partial \xi}+\frac{\partial u}{\partial \eta}\frac{\partial \eta}{\partial x}+\frac{\partial v}{\partial \kappa}+\frac{\partial v}{\partial \eta}\frac{\partial \eta}{\partial y}\right)\right\}, \tag{C12}$$

$$\frac{\partial r_{xy}}{\partial t} = -\frac{1}{\tau_\sigma}\left\{ r_{xy} + \mu\left(\frac{\tau_\varepsilon^S}{\tau_\sigma}-1\right)\left(\frac{\partial u}{\partial \kappa}+\frac{\partial u}{\partial \eta}\frac{\partial \eta}{\partial y}+\frac{\partial v}{\partial \xi}+\frac{\partial v}{\partial \eta}\frac{\partial \eta}{\partial x}\right)\right\}, \tag{C13}$$

$$\frac{\partial r_{xz}}{\partial t} = -\frac{1}{\tau_\sigma}\left\{ r_{xz} + \mu\left(\frac{\tau_\varepsilon^S}{\tau_\sigma}-1\right)\left(\frac{\partial u}{\partial \eta}\frac{\partial \eta}{\partial z}+\frac{\partial w}{\partial \xi}+\frac{\partial w}{\partial \eta}\frac{\partial \eta}{\partial x}\right)\right\}, \tag{C14}$$

$$\frac{\partial r_{yz}}{\partial t} = -\frac{1}{\tau_\sigma}\left\{ r_{yz} + \mu\left(\frac{\tau_\varepsilon^S}{\tau_\sigma}-1\right)\left(\frac{\partial v}{\partial \eta}\frac{\partial \eta}{\partial z}+\frac{\partial w}{\partial \kappa}+\frac{\partial w}{\partial \eta}\frac{\partial \eta}{\partial y}\right)\right\}. \tag{C15}$$

Substituting for $\partial\eta/\partial x$, $\partial\eta/\partial y$ and $\partial\eta/\partial z$ from eqs (24)–(28), we obtain the medium eqs (29)–(43).

APPENDIX D: BOUNDARY CONDITIONS

Assume that a velocity vector **v** with components u, v and w is given in a Cartesian (x, y, z)-coordinate system with basis vectors **i**, **j** and **k**. This system is then rotated through angles (θ, ϕ) into a new (x', y', z')-coordinate system with basis vectors **i**′, **j**′ and **k**′. θ is the rotation angle between the x-axis and the x'-axis in the (x, z)-plane and ϕ is the rotation angle between the y-axis and the y'-axis in the (y', z')-plane. In this new system the vector **v** is denoted by **v**′ with components u', v' and w'. We then have the relationships

$$\begin{pmatrix}\mathbf{i}' \\ \mathbf{j}' \\ \mathbf{k}'\end{pmatrix} = \mathbf{A}\begin{pmatrix}\mathbf{i} \\ \mathbf{j} \\ \mathbf{k}\end{pmatrix}, \tag{D1}$$

where **A** is the rotation matrix given by eq. (48). Correspondingly,

$$\begin{pmatrix}\mathbf{i} \\ \mathbf{j} \\ \mathbf{k}\end{pmatrix} = \mathbf{A}^{-1}\begin{pmatrix}\mathbf{i}' \\ \mathbf{j}' \\ \mathbf{k}'\end{pmatrix} = \mathbf{A}^{\mathrm{T}}\begin{pmatrix}\mathbf{i}' \\ \mathbf{j}' \\ \mathbf{k}'\end{pmatrix}, \tag{D2}$$

where $\mathbf{A}^{-1}$ and $\mathbf{A}^{\mathrm{T}}$ are equal (since **A** is orthogonal) and the inverse and transpose of **A** respectively.

Using the computational grid coordinates (ξ, κ, η) instead of the Cartesian (x, y, z)-system and

$$|\mathbf{n}| = \sqrt{\left(\frac{\partial z_0}{\partial \xi}\right)^2 + \left(\frac{\partial z_0}{\partial \kappa}\right)^2 + 1}\,,$$

a unit normal vector to a surface topography element can be written as

$$\hat{\mathbf{n}} = \frac{\mathbf{n}}{|\mathbf{n}|} = \frac{1}{|\mathbf{n}|}\left(-\frac{\partial z_0(\xi, \kappa)}{\partial \xi}, -\frac{\partial z_0(\xi, \kappa)}{\partial \kappa}, 1\right)^{\mathrm{T}}$$

$$= (-\cos\phi\sin\theta, -\sin\phi, \cos\phi\cos\theta)^{\mathrm{T}} \tag{D3}$$

with our choice of rotation angles. From this we obtain

$$\frac{\tan\phi}{\cos\theta} = \frac{\partial z_0(\xi, \kappa)}{\partial \kappa}, \quad \text{i.e. } \tan\phi = \frac{\partial z_0(\xi, \kappa)}{\partial \kappa}\cos\theta, \tag{D4}$$

$$\cos\phi = \cos\left[\arctan\left(\frac{\partial z_0(\xi, \kappa)}{\partial \kappa}\cos\theta\right)\right] \tag{D5}$$

and

$$\sin\phi = \sin\left[\arctan\left(\frac{\partial z_0(\xi, \kappa)}{\partial \kappa}\cos\theta\right)\right]. \tag{D6}$$

The coordinate transformation for $\mathbf{v}$ is given by $\mathbf{v} = \mathbf{A}^{-1}\mathbf{v}'$, or $\mathbf{v}' = \mathbf{A}\mathbf{v}$. Component-wise this is

$$u' = (\cos\theta)u + (\sin\theta)w, \tag{D7}$$

$$v' = -(\sin\theta\sin\phi)u + (\cos\phi)v + (\cos\theta\sin\phi)w, \tag{D8}$$

$$w' = -(\sin\theta\cos\phi)u - (\sin\phi)v + (\cos\theta\cos\phi)w. \tag{D9}$$

Applying the chain rule to a differentiable function f, we obtain

$$\frac{\partial f}{\partial x'} = \frac{\partial f}{\partial x}\frac{\partial x}{\partial x'} + \frac{\partial f}{\partial y}\frac{\partial y}{\partial x'} + \frac{\partial f}{\partial z}\frac{\partial z}{\partial x'} = \frac{\partial f}{\partial x}\cos\theta + \frac{\partial f}{\partial z}\sin\theta, \tag{D10}$$

$$\frac{\partial f}{\partial y'} = \frac{\partial f}{\partial x}\frac{\partial x}{\partial y'} + \frac{\partial f}{\partial y}\frac{\partial y}{\partial y'} + \frac{\partial f}{\partial z}\frac{\partial z}{\partial y'}$$
$$= \frac{\partial f}{\partial x}(-\sin\theta\sin\phi) + \frac{\partial f}{\partial y}\cos\phi + \frac{\partial f}{\partial z}\cos\theta\sin\phi, \tag{D11}$$

$$\frac{\partial f}{\partial z'} = \frac{\partial f}{\partial x}\frac{\partial x}{\partial z'} + \frac{\partial f}{\partial y}\frac{\partial y}{\partial z'} + \frac{\partial f}{\partial z}\frac{\partial z}{\partial z'}$$
$$= \frac{\partial f}{\partial x}(-\sin\theta\cos\phi) + \frac{\partial f}{\partial y}(-\sin\phi) + \frac{\partial f}{\partial z}\cos\theta\cos\phi. \tag{D12}$$

The last equalities are obtained from eq. (D2). The free boundary conditions (44)–(46) for the velocities have to be enforced in the local (x', y', z')-system, where the z'-axis is normal to the surface at the local point, i.e.

$$\frac{\partial u'}{\partial z'} = -\frac{\partial w'}{\partial x'}, \tag{D13}$$

$$\frac{\partial v'}{\partial z'} = -\frac{\partial w'}{\partial y'}, \tag{D14}$$

$$\frac{\partial w'}{\partial z'} = -\frac{\lambda}{\lambda + 2\mu}\left(\frac{\partial u'}{\partial x'} + \frac{\partial v'}{\partial y'}\right). \tag{D15}$$

If the chain rule is applied as above, we obtain

$$\frac{\partial u'}{\partial x}(-\sin\theta\cos\phi) + \frac{\partial u'}{\partial y}(-\sin\phi) + \frac{\partial u'}{\partial z}\cos\theta\cos\phi = -\frac{\partial w'}{\partial x}\cos\theta - \frac{\partial w'}{\partial z}\sin\theta, \tag{D16}$$

$$\frac{\partial v'}{\partial x}(-\sin\theta\cos\phi) + \frac{\partial v'}{\partial y}(-\sin\phi) + \frac{\partial v'}{\partial z}\cos\theta\cos\phi = -\frac{\partial w'}{\partial x}(-\sin\theta\sin\phi) - \frac{\partial w'}{\partial y}\cos\phi - \frac{\partial w'}{\partial z}\cos\theta\sin\phi, \tag{D17}$$

$$\frac{\partial w'}{\partial x}(-\sin\theta\cos\phi) + \frac{\partial w'}{\partial y}(-\sin\phi) + \frac{\partial w'}{\partial z}\cos\theta\cos\phi$$
$$= -\frac{\lambda}{\lambda+2\mu}\left(\frac{\partial u'}{\partial x}\cos\theta + \frac{\partial u'}{\partial z}\sin\theta + \frac{\partial v'}{\partial x}(-\sin\theta\sin\phi) + \frac{\partial v'}{\partial y}\cos\phi + \frac{\partial v'}{\partial z}\cos\theta\sin\phi\right). \tag{D18}$$

Now we apply the above expressions for u', v' and w' that were obtained from the rotation. This leads to

$$\left[\cos\theta\frac{\partial u}{\partial x} + \sin\theta\frac{\partial w}{\partial x}\right](-\sin\theta\cos\phi) + \left[\cos\theta\frac{\partial u}{\partial y} + \sin\theta\frac{\partial w}{\partial y}\right](-\sin\phi) + \left[\cos\theta\frac{\partial u}{\partial z} + \sin\theta\frac{\partial w}{\partial z}\right]\cos\theta\cos\phi$$
$$= \left[\sin\theta\cos\phi\frac{\partial u}{\partial x} + \sin\phi\frac{\partial v}{\partial x} - \cos\theta\cos\phi\frac{\partial w}{\partial x}\right]\cos\theta + \left[\sin\theta\cos\phi\frac{\partial u}{\partial z} + \sin\phi\frac{\partial v}{\partial z} - \cos\theta\cos\phi\frac{\partial w}{\partial z}\right]\sin\theta, \tag{D19}$$

$$\left[-\sin\theta\sin\phi\frac{\partial u}{\partial x} + \cos\phi\frac{\partial v}{\partial x} + \cos\theta\sin\phi\frac{\partial w}{\partial x}\right](-\sin\theta\cos\phi) + \left[-\sin\theta\sin\phi\frac{\partial u}{\partial y} + \cos\phi\frac{\partial v}{\partial y} + \cos\theta\sin\phi\frac{\partial w}{\partial y}\right](-\sin\phi)$$
$$+ \left[-\sin\theta\sin\phi\frac{\partial u}{\partial z} + \cos\phi\frac{\partial v}{\partial z} + \cos\theta\sin\phi\frac{\partial w}{\partial z}\right]\cos\theta\cos\phi$$
$$= \left[\sin\theta\cos\phi\frac{\partial u}{\partial x} + \sin\phi\frac{\partial v}{\partial x} - \cos\theta\cos\phi\frac{\partial w}{\partial x}\right](-\sin\theta\sin\phi) + \left[\sin\theta\cos\phi\frac{\partial u}{\partial y} + \sin\phi\frac{\partial v}{\partial y} - \cos\theta\cos\phi\frac{\partial w}{\partial y}\right]\cos\phi$$
$$+ \left[\sin\theta\cos\phi\frac{\partial u}{\partial z} + \sin\phi\frac{\partial v}{\partial z} - \cos\theta\cos\phi\frac{\partial w}{\partial z}\right]\cos\theta\sin\phi, \tag{D20}$$

$$
\left[-\sin\theta\cos\phi\,\frac{\partial u}{\partial x}-\sin\phi\,\frac{\partial v}{\partial x}+\cos\theta\cos\phi\,\frac{\partial w}{\partial x}\right](-\sin\theta\cos\phi)+\left[-\sin\theta\cos\phi\,\frac{\partial u}{\partial y}-\sin\phi\,\frac{\partial v}{\partial y}+\cos\theta\cos\phi\,\frac{\partial w}{\partial y}\right](-\sin\phi)
$$

$$
+\left[-\sin\theta\cos\phi\,\frac{\partial u}{\partial z}-\sin\phi\,\frac{\partial v}{\partial z}+\cos\theta\cos\phi\,\frac{\partial w}{\partial z}\right]\cos\theta\cos\phi
$$

$$
=-\frac{\lambda}{\lambda+2\mu}\left\{\left[\cos\theta\,\frac{\partial u}{\partial x}+\sin\theta\,\frac{\partial w}{\partial x}\right]\cos\theta+\left[\cos\theta\,\frac{\partial u}{\partial z}+\sin\theta\,\frac{\partial w}{\partial z}\right]\sin\theta\right.
$$

$$
+\left[-\sin\theta\sin\phi\,\frac{\partial u}{\partial x}+\cos\phi\,\frac{\partial v}{\partial x}+\cos\theta\sin\phi\,\frac{\partial w}{\partial x}\right](-\sin\theta\sin\phi)+\left[-\sin\theta\sin\phi\,\frac{\partial u}{\partial y}+\cos\phi\,\frac{\partial v}{\partial y}+\cos\theta\sin\phi\,\frac{\partial w}{\partial y}\right]\cos\phi
$$

$$
+\left.\left[-\sin\theta\sin\phi\,\frac{\partial u}{\partial z}+\cos\phi\,\frac{\partial v}{\partial z}+\cos\theta\sin\phi\,\frac{\partial w}{\partial z}\right]\cos\theta\sin\phi\right\}. \tag{D21}
$$

We divide the first of these equations by $\cos^2\theta\cos\phi$, the second by $\cos\theta\cos^2\phi$ and the third by $\cos^2\theta\cos^2\phi$. These divisions assume $\theta\neq\pm\pi/2$ and $\phi\neq\pm\pi/2$. This means that the topography cannot have vertical sections along the planes of rotation, that is, the topography function must be single-valued. This is a reasonable assumption given that the topography function $z_0(\xi,\kappa)$ is assumed to be smooth. After restructuring, the three equations become

$$
(1-\tan^2\theta)\,\frac{\partial u}{\partial z}-\frac{\tan\theta}{\cos\theta}\tan\phi\,\frac{\partial v}{\partial z}+2\tan\theta\,\frac{\partial w}{\partial z}=2\tan\theta\,\frac{\partial u}{\partial x}+\frac{\tan\phi}{\cos\theta}\,\frac{\partial v}{\partial x}+(\tan^2\theta-1)\,\frac{\partial w}{\partial x}+\frac{\tan\phi}{\cos\theta}\,\frac{\partial u}{\partial y}+\frac{\tan\theta}{\cos\theta}\tan\phi\,\frac{\partial w}{\partial y}, \tag{D22}
$$

$$
-2\sin\theta\tan\phi\,\frac{\partial u}{\partial z}+(1-\tan^2\phi)\,\frac{\partial v}{\partial z}+2\cos\theta\tan\phi\,\frac{\partial w}{\partial z}=-2\sin\theta\tan\theta\tan\phi\,\frac{\partial u}{\partial x}+\tan\theta(1-\tan^2\phi)\,\frac{\partial v}{\partial x}+2\sin\theta\tan\phi\,\frac{\partial w}{\partial x}
$$

$$
+\tan\theta(1-\tan^2\phi)\,\frac{\partial u}{\partial y}+2\,\frac{\tan\phi}{\cos\theta}\,\frac{\partial v}{\partial y}+(\tan^2\phi-1)\,\frac{\partial w}{\partial y}, \tag{D23}
$$

$$
\tan\theta\left\{\frac{\lambda}{\lambda+2\mu}\left(\frac{1}{\cos^2\phi}-\tan^2\phi\right)-1\right\}\frac{\partial u}{\partial z}+\frac{\tan\phi}{\cos\theta}\left\{\frac{\lambda}{\lambda+2\mu}-1\right\}\frac{\partial v}{\partial z}+\left\{\frac{\lambda}{\lambda+2\mu}\left(\frac{\tan^2\theta}{\cos^2\phi}+\tan^2\phi\right)+1\right\}\frac{\partial w}{\partial z}
$$

$$
=\left\{-\frac{\lambda}{\lambda+2\mu}\left(\frac{1}{\cos^2\phi}+\tan^2\theta\tan^2\phi\right)-\tan^2\theta\right\}\frac{\partial u}{\partial x}+\frac{\tan\theta}{\cos\theta}\tan\phi\left\{\frac{\lambda}{\lambda+2\mu}-1\right\}\frac{\partial v}{\partial x}+\tan\theta\left\{\frac{\lambda}{\lambda+2\mu}\left(\tan^2\phi-\frac{1}{\cos^2\phi}\right)+1\right\}\frac{\partial w}{\partial x}
$$

$$
+\frac{\tan\theta}{\cos\theta}\tan\phi\left\{\frac{\lambda}{\lambda+2\mu}-1\right\}\frac{\partial u}{\partial y}-\frac{1}{\cos^2\theta}\left\{\frac{\lambda}{\lambda+2\mu}+\tan^2\phi\right\}\frac{\partial v}{\partial y}+\frac{\tan\phi}{\cos\theta}\left\{1-\frac{\lambda}{\lambda+2\mu}\right\}\frac{\partial w}{\partial y}. \tag{D24}
$$

The equations are now given in the Cartesian (x,y,z)-system. However, as for the medium equations, we require that the Cartesian equations in x, y and z be valid inside the curved grid whose surface coincides with the surface topography in the Cartesian system. We must thus find the appearance of these equations in the rectangular (ξ,κ,η)-grid where the numerical computations are performed. This results in curved grid equations given in the (ξ,κ,η)-grid. We must therefore apply the chain rule to the boundary conditions in the same way as was done for the medium equations.

At the free surface $\eta=\eta_{\max}$, and with $\partial z_0(\xi,\kappa)/\partial\xi=\tan\theta$ and $\partial z_0(\xi,\kappa)/\partial\kappa=\tan\phi/\cos\theta$ [now using the computational (ξ,κ,η)-grid], eqs (26) and (27) become

$$
A(\xi,\kappa,\eta)=\frac{\partial\eta}{\partial x}=-\frac{\eta_{\max}}{z_0(\xi,\kappa)}\tan\theta=-C(\xi,\kappa)\tan\theta, \tag{D25}
$$

$$
B(\xi,\kappa,\eta)=\frac{\partial\eta}{\partial y}=-\frac{\eta_{\max}}{z_0(\xi,\kappa)}\frac{\tan\phi}{\cos\theta}=-C(\xi,\kappa)\frac{\tan\phi}{\cos\theta}. \tag{D26}
$$

Eqs (21)–(23) for a differentiable function $f(x,y,z)$ at the surface then become

$$
\frac{\partial f}{\partial x}=\frac{\partial f}{\partial\xi}-C(\xi,\kappa)\tan\theta\,\frac{\partial f}{\partial\eta}, \tag{D27}
$$

$$
\frac{\partial f}{\partial y}=\frac{\partial f}{\partial\kappa}-C(\xi,\kappa)\frac{\tan\phi}{\cos\theta}\,\frac{\partial f}{\partial\eta}, \tag{D28}
$$

$$
\frac{\partial f}{\partial z}=C(\xi,\kappa)\frac{\partial f}{\partial\eta}. \tag{D29}
$$

When this is used in the boundary conditions, together with $\zeta = \lambda/(\lambda+2\mu)$, we obtain

$$(1-\tan^2\theta)\,C(\xi,\kappa)\frac{\partial u}{\partial \eta} - \frac{\tan\theta}{\cos\theta}\tan\phi\, C(\xi,\kappa)\frac{\partial v}{\partial \eta} + 2\tan\theta\, C(\xi,\kappa)\frac{\partial w}{\partial \eta}$$

$$= 2\tan\theta\left(\frac{\partial u}{\partial \xi} - C(\xi,\kappa)\tan\theta\frac{\partial u}{\partial \eta}\right) + \frac{\tan\phi}{\cos\theta}\left(\frac{\partial v}{\partial \xi} - C(\xi,\kappa)\tan\theta\frac{\partial v}{\partial \eta}\right) + (\tan^2\theta-1)\left(\frac{\partial w}{\partial \xi} - C(\xi,\kappa)\tan\theta\frac{\partial w}{\partial \eta}\right)$$

$$+ \frac{\tan\phi}{\cos\theta}\left(\frac{\partial u}{\partial \kappa} - C(\xi,\kappa)\frac{\tan\phi}{\cos\theta}\frac{\partial u}{\partial \eta}\right) + \frac{\tan\theta}{\cos\theta}\tan\phi\left(\frac{\partial w}{\partial \kappa} - C(\xi,\kappa)\frac{\tan\phi}{\cos\theta}\frac{\partial w}{\partial \eta}\right), \tag{D30}$$

$$-2\sin\theta\tan\phi\, C(\xi,\kappa)\frac{\partial u}{\partial \eta} + (1-\tan^2\phi)\,C(\xi,\kappa)\frac{\partial v}{\partial \eta} + 2\cos\theta\tan\phi\, C(\xi,\kappa)\frac{\partial w}{\partial \eta}$$

$$= -2\sin\theta\tan\theta\tan\phi\left(\frac{\partial u}{\partial \xi} - C(\xi,\kappa)\tan\theta\frac{\partial u}{\partial \eta}\right) + \tan\theta(1-\tan^2\phi)\left(\frac{\partial v}{\partial \xi} - C(\xi,\kappa)\tan\theta\frac{\partial v}{\partial \eta}\right)$$

$$+ 2\sin\theta\tan\phi\left(\frac{\partial w}{\partial \xi} - C(\xi,\kappa)\tan\theta\frac{\partial w}{\partial \eta}\right) + \tan\theta(1-\tan^2\phi)\left(\frac{\partial u}{\partial \kappa} - C(\xi,\kappa)\frac{\tan\phi}{\cos\theta}\frac{\partial u}{\partial \eta}\right) + 2\frac{\tan\phi}{\cos\theta}\left(\frac{\partial v}{\partial \kappa} - C(\xi,\kappa)\frac{\tan\phi}{\cos\theta}\frac{\partial v}{\partial \eta}\right)$$

$$+ (\tan^2\phi-1)\left(\frac{\partial w}{\partial \kappa} - C(\xi,\kappa)\frac{\tan\phi}{\cos\theta}\frac{\partial w}{\partial \eta}\right), \tag{D31}$$

$$\tan\theta\{\zeta-1\}C(\xi,\kappa)\frac{\partial u}{\partial \eta} + \frac{\tan\phi}{\cos\theta}\{\zeta-1\}C(\xi,\kappa)\frac{\partial v}{\partial \eta} + \left\{\zeta\left(\frac{\tan^2\theta}{\cos^2\phi}+\tan^2\phi\right)+1\right\}C(\xi,\kappa)\frac{\partial w}{\partial \eta}$$

$$= \left\{-\zeta\left(\frac{1}{\cos^2\phi}+\tan^2\theta\tan^2\phi\right)-\tan^2\theta\right\}\left(\frac{\partial u}{\partial \xi} - C(\xi,\kappa)\tan\theta\frac{\partial u}{\partial \eta}\right) + \frac{\tan\theta}{\cos\theta}\tan\phi\{\zeta-1\}\left(\frac{\partial v}{\partial \xi} - C(\xi,\kappa)\tan\theta\frac{\partial v}{\partial \eta}\right)$$

$$- \tan\theta\{\zeta-1\}\left(\frac{\partial w}{\partial \xi} - C(\xi,\kappa)\tan\theta\frac{\partial w}{\partial \eta}\right) + \frac{\tan\theta}{\cos\theta}\tan\phi\{\zeta-1\}\left(\frac{\partial u}{\partial \kappa} - C(\xi,\kappa)\frac{\tan\phi}{\cos\theta}\frac{\partial u}{\partial \eta}\right)$$

$$- \frac{1}{\cos^2\theta}\{\zeta+\tan^2\phi\}\left(\frac{\partial v}{\partial \kappa} - C(\xi,\kappa)\frac{\tan\phi}{\cos\theta}\frac{\partial v}{\partial \eta}\right) - \frac{\tan\phi}{\cos\theta}\{\zeta-1\}\left(\frac{\partial w}{\partial \kappa} - C(\xi,\kappa)\frac{\tan\phi}{\cos\theta}\frac{\partial w}{\partial \eta}\right). \tag{D32}$$

Rearranging terms and using the trigonometric simplifications

$$2\cos\theta + 2\sin\theta\tan\theta + \frac{1}{\cos\theta}(\tan^2\phi-1) = \frac{1}{\cos\theta}(1+\tan^2\phi), \tag{D33}$$

$$-2 - 2\tan^2\theta + \frac{1}{\cos^2\theta}(1-\tan^2\phi) = -\frac{1}{\cos^2\theta}(1+\tan^2\phi), \tag{D34}$$

$$1 + \tan^2\theta + \frac{\tan^2\phi}{\cos^2\theta} = \frac{1}{\cos^2\theta}(1+\tan^2\phi), \tag{D35}$$

$$(1+\tan^2\theta)(1-\tan^2\phi) + 2\frac{\tan^2\phi}{\cos^2\theta} = \frac{1}{\cos^2\theta}(1+\tan^2\phi) \tag{D36}$$

leads to the equations

$$\frac{1}{\cos^2\theta}(1+\tan^2\phi)C(\xi,\kappa)\frac{\partial u}{\partial \eta} + \frac{1}{\cos^2\theta}(1+\tan^2\phi)\tan\theta\, C(\xi,\kappa)\frac{\partial w}{\partial \eta} = 2\tan\theta\frac{\partial u}{\partial \xi} + \frac{\tan\phi}{\cos\theta}\frac{\partial v}{\partial \xi} + (\tan^2\theta-1)\frac{\partial w}{\partial \xi} + \frac{\tan\phi}{\cos\theta}\frac{\partial u}{\partial \kappa}$$

$$+ \frac{\tan\theta}{\cos\theta}\tan\phi\frac{\partial w}{\partial \kappa}, \tag{D37}$$

$$-\frac{1}{\cos^2\theta}(1+\tan^2\phi)\sin\theta\tan\phi\, C(\xi,\kappa)\frac{\partial u}{\partial \eta} + \frac{1}{\cos^2\theta}(1+\tan^2\phi)C(\xi,\kappa)\frac{\partial v}{\partial \eta} + \frac{1}{\cos\theta}(1+\tan^2\phi)\tan\phi\, C(\xi,\kappa)\frac{\partial w}{\partial \eta}$$

$$= -2\sin\theta\tan\theta\tan\phi\frac{\partial u}{\partial \xi} + \tan\theta(1-\tan^2\phi)\frac{\partial v}{\partial \xi} + 2\sin\theta\tan\phi\frac{\partial w}{\partial \xi} + \tan\theta(1-\tan^2\phi)\frac{\partial u}{\partial \kappa} + 2\frac{\tan\phi}{\cos\theta}\frac{\partial v}{\partial \kappa} + (\tan^2\phi-1)\frac{\partial w}{\partial \kappa}, \tag{D38}$$

$$\left\{ \left(1 + \frac{\tan^2 \phi}{\cos^2 \theta}\right)(\zeta - 1) - \zeta\left(\frac{1}{\cos^2 \phi} + \tan^2 \theta \tan^2 \phi\right) - \tan^2 \theta \right\} \tan \theta \, C(\xi, \kappa) \frac{\partial u}{\partial \eta}$$

$$+ \left\{ (1 + \tan^2 \theta)(\zeta - 1) - \frac{1}{\cos^2 \theta}(\zeta + \tan^2 \phi) \right\} \frac{\tan \phi}{\cos \theta} \, C(\xi, \kappa) \frac{\partial v}{\partial \eta}$$

$$+ \left\{ \zeta\left(\frac{\tan^2 \theta}{\cos^2 \phi} + \tan^2 \phi\right) + 1 - \left(\tan^2 \theta + \frac{\tan^2 \phi}{\cos^2 \theta}\right)(\zeta - 1) \right\} C(\xi, \kappa) \frac{\partial w}{\partial \eta}$$

$$= \left\{ -\zeta\left(\frac{1}{\cos^2 \phi} + \tan^2 \theta \tan^2 \phi\right) - \tan^2 \theta \right\} \frac{\partial u}{\partial \xi} + \frac{\tan \theta}{\cos \theta} \tan \phi (\zeta - 1) \frac{\partial v}{\partial \xi} - \tan \theta (\zeta - 1) \frac{\partial w}{\partial \xi} + \frac{\tan \theta}{\cos \theta} \tan \phi (\zeta - 1) \frac{\partial u}{\partial \kappa}$$

$$- \frac{1}{\cos^2 \theta}(\zeta + \tan^2 \phi) \frac{\partial v}{\partial \kappa} - \frac{\tan \phi}{\cos \theta}(\zeta - 1) \frac{\partial w}{\partial \kappa}. \tag{D39}$$

Finally, I simplify expressions by using the trigonometric relations

$$1 + \frac{\tan^2 \phi}{\cos^2 \theta} = \frac{1}{\cos^2 \phi} + \tan^2 \theta \tan^2 \phi, \tag{D40}$$

$$\frac{\tan^2 \theta}{\cos^2 \phi} + \tan^2 \phi = \frac{\tan^2 \phi}{\cos^2 \theta} + \tan^2 \theta, \tag{D41}$$

and use the relations $\tan \theta = \partial z_0(\xi, \kappa)/\partial \xi$, $\tan \phi = \partial z_0(\xi, \kappa)/\partial \kappa \cos \theta$ and the definitions (52)–(56). This leads to the closed set of boundary conditions for the particle velocities at a free-surface topography, (49)–(51).